https://doi.org/10.5194/egusphere-2026-2575
Preprint. Discussion started: 26 May 2026

Optical properties and global distribution of the Hunga aerosols 2022 observed by Aeolus and atmospheric lidars: new insights into the vertical sedimentation of stratospheric sulfate plumes

Dimitri Trapon[1], Holger Baars[1], Sebastian Bley[1], Albert Ansmann[1], Michael Rennie[2], Sergey Khaykin[3], and Michael Sicard[4,5]

[1]Leibniz Institute for Tropospheric Research (TROPOS), Remote Sensing of Atmospheric Processes Department, Leipzig, Germany
[2]European Centre for Medium-Range Weather Forecasts, Research Department, Reading, United Kingdom
[3]Laboratoire Atmosphère Observations Spatiales (LATMOS), CNRS, Sorbonne University, Guyancourt, France
[4]Laboratoire de l'Atmosphère et des Cyclones (LACy), Saint-Denis de la Réunion, France
[5]CommSensLab, Department of Signal Theory and Communications, Universitat Politècnica de Catalunya, Barcelona, Spain

Correspondence: Dimitri Trapon (dimitri.trapon@tropos.de)

Abstract. Stratospheric aerosol plumes from the 2022 Hunga eruption were observed by the first-ever ultraviolet (UV) 355 nm Doppler and High Spectral Resolution Lidar (HSRL) on board the European Space Agency's Aeolus satellite. Independent measurement of extinction and co-polarized backscatter coefficients for particles are shown, capturing the Hunga plumes up to ≈ 28 km in altitude by 24 January 2022. Global map of L2A product are produced for latitudes band up to [35° S–10° N]. They are analysed with weekly average of sulfur dioxide (SO_2) concentration and sulfate aerosol (SA) optical depth (OD) from spaceborne measurement. A plume composed of optically thick patches with high SA OD above 0.025 is captured above 26 km in altitude. It exhibits high UV signal extinction up to ≈ 350 $\mathrm{Mm^{-1}}$, scattering ratio (SR) up to ≈ 40, local optical depth (LOD) above 0.2, and lidar ratio (LR) above 100 sr. These SA long-lived patches are observed drifting South and transported West. Two branches separate by mid February 2022: a southern tale at ≈ 25 to 27 km in altitude around latitudes [30° S–15° S] and a northern tale at ≈ 23 to 25 km in altitude around latitudes [15° S–10° N]. The Aeolus LR and LOD reach lower values for the aging branches, i.e. below 80 sr and 0.04 respectively. A short-lived plume with low SA OD and high SO_2 concentration is observed at lower altitudes ≈ 18 to 22 km with less strong UV scattering properties, and appears to disaggregate quickly.

1 Introduction

The ESA Aeolus satellite was successfully operated between 22 August 2018 and 30 April 2023 carrying the Atmospheric LAser Doppler INstrument (ALADIN), the first Doppler Wind Lidar in space, which was emitting ultraviolet (UV) laser pulses at 355 nm in off-NADIR mode $\approx 35°$ (Reitebuch et al., 2024). Aeolus flew in sun-synchronous orbit at ≈ 320 km in altitude with revisit time of 7 days (i.e. ≈ 15 orbits per day, a global coverage being achieved each week with ≈ 105 orbits) and crossing the equator at local solar times of $\approx$ 06:00 (descending node) and $\approx$ 18:00 (ascending node). The ALADIN lidar comes with High Spectral Resolution (HSR) capacity, then measuring the signal from molecules (Rayleigh channel) and particles (Mie

https://doi.org/10.5194/egusphere-2026-2575
Preprint. Discussion started: 26 May 2026

channel) with the possibility to distinguish both contributions. The instrument was initially designed to provide wind speed at global scale from the Earth's surface up to the lower stratosphere (≈ 25 km to 30 km in altitude) (Flamant et al., 2008; Dabas et al., 2008), but it was also measuring vertical profiling of thin clouds and aerosols' optical properties with 24 range bins of thickness from 250 m to 2 km. Both the range bin thickness and the maximum height of the measurement were adjustable. This allowed to observe aerosol layers up to 30 km in altitude. Independent measurement of co-polarized backscatter and extinction coefficients for particles (Flamant et al., 2008) are comprised in the Level-2A (L2A) product (Flamant et al., 2022; Trapon et al., 2022). Coupled with the good 7-days revisit cycle, they are particularly relevant for tracking long-range transported aerosols (Sun et al., 2026), even in the tropics and above oceans where ground-based measurement are limited. The HSR capacity represents a real added value compared to other atmospheric lidars: the particles extinction-to-backscatter ratio, so-called lidar ratio (LR), is then not fixed. As the LR depends on particles shape, size and microphysical properties, it is often used for aerosol classification (Floutsi et al., 2023).

Aeolus can contribute to the observations of the reported stratospheric aerosol perturbation induced by the Hunga 2022 volcanic eruption (Sellitto et al., 2022, 2024a). On 15 January 2022 the submarine Hunga Tonga-Hunga Ha'apai volcano (20.54° S, 175.38° W) located in southwest Pacific Ocean erupted with a high-magnitude volcanic explosion. Particles have been injected in high altitudes up to the mesosphere ≈ 50 km before falling back to the stratosphere with long-term persistence (Schoeberl et al., 2024; Sicard et al., 2025). Spaceborne observations by the Cloud-Aerosol Lidar with Orthogonal Polarization (CALIOP) instrument (Winker et al., 2004) on board CALIPSO satellite (Vaughan et al., 2004) have been widely used to characterize the early Hunga plume (Legras et al., 2022; Khaykin et al., 2022). Aerosol layers from the main plume were circumnavigating the Earth, stabilizing around 25 km to 27 km in altitude by late January 2022 (Khaykin et al., 2022). But unlike ALADIN, CALIOP does not have HSR. It is a two-wavelength elastic lidar operating at 532 nm and 1064 nm that detects total backscatter and therefore does not distinguish the contributions from molecules and particles (Winker et al., 2006), hence some ambiguities in cloud and aerosol properties. The use of a-priori information on aerosol subtype taken from other sources including models (Winker et al., 2006) is required for the derivation of the optical properties and the LR is not constrained (Winker et al., 2004). Efforts have been made to derive the 532 nm LR from CALIOP local optical depth (LOD) and attenuated backscatter with iterative method using approximations, showing values above 80 sr for the early plumes at ≈ 30 km height and stabilizing to 40 sr ± 20 after few weeks (Duchamp et al., 2026). The calculation assumes no vertical or horizontal gradient of LR inside the plume, then considering uniform microphysical properties for the particles (Duchamp et al., 2026). But unusual aerosol size distribution have been observed (Sellitto et al., 2022). It is assumed to be related to the fast conversion of sulfur dioxide (SO_2) to sulfuric acid droplets H_2SO_4 (Bruckert et al., 2025; Sellitto et al., 2024b) that nucleate to sulfate aerosols (SA), the process being enhanced by abundant water (Millán et al., 2022; Zhu et al., 2022). Balloon measurements from the Tonga volcano Rapid Response Experiment (TR2Ex) conducted in south-west Indian Ocean at La Reunion also showed gradient in optical properties with overall high signal in aerosol extinction, suggesting differences in shape and microphysical properties from the top plume above 27 km altitude when compared to the inner core plume (Asher et al., 2023). Overall, these studies outline a critical role of water vapour in the rapid SA formation, highlighting differences in SO_2 and SA concentrations for the different Hunga clouds circumnavigating the Earth at different altitudes (Zhu et al., 2025). But large uncertainties have been reported in

https://doi.org/10.5194/egusphere-2026-2575
Preprint. Discussion started: 26 May 2026

the assumptions of SO_2 plume altitude (Xia et al., 2024) and the topic remains an active area of research (Zhu et al., 2025). Aeolus therefore provides valuable representative 355 nm LR and particles extinction coefficient in such conditions, i.e. high altitudes with strong signal-to-noise ratio (SNR) from mainly spherical particles (Asher et al., 2023), with low depolarization ratio below 2 % (Legras et al., 2022; Taha et al., 2022) which makes the cross-polarized component of the backscatter light missed by Aeolus negligible. The occurrence of dense water clouds and aerosol layers from other sources is also expected to be minimal in Upper Troposphere and Lower Stratosphere (UTLS), making the detection and tracking of the Hunga plume with Aeolus easier. Moreover, the aerosol effective radius measured for the main Hunga plumes above 24 km altitude reached $\approx$ 0.3 to 0.4 µm (Knepp et al., 2024), making the Aeolus UV signal at 355 nm a good candidate for analysis due to its greater sensitivity to these sub-micron particles than higher wavelengths.

In this paper, the Aeolus L2A product are briefly introduced and the ability of ALADIN to track stratospheric aerosols is demonstrated firstly showing early observations of the Hunga aerosols with single overpasses. They are compared with ground-based and space-borne lidars between 25 January 2022 and 01 February 2022. Then, weekly global maps of Aeolus L2A product are shown for the ageing plumes until 06 March 2022. The maps are analysed in parallel to SO_2 and SA data. Two-dimensional histograms of L2A extinction versus backscatter coefficients are presented and illustrate the particles height and UV scattering properties over time. A final section encloses the paper, discussing the added values of the Aeolus observations in context of the global Hunga aerosol analysis. Descriptions of the dataset used for the study can be found in the Appendix (A1).

2 Aeolus aerosol product

2.1 The SCA and MLEsub algorithms and their quality flagging

The present study uses the Aeolus L2A product retrieved with the standard correct algorithm (SCA) and the maximum likelihood algorithm (MLE). They have been processed with processor version 16, and are labelled Baseline 16. The SCA makes use of the matching between the Rayleigh and Mie channels to invert the lidar equations (Flament et al., 2021; Trapon et al., 2025). Among other products it provides the attenuated backscatter coefficients for molecules $\beta^{\text{att}}_{\text{mol}}$ and particles $\beta^{\text{att}}_{\text{part}}$ at finer resolution referred as measurement (i.e. lidar signal accumulation down to $\approx$ 6 km in the horizontal direction for the period 13 December 2021 to 04 April 2022). The two products can be added together to get the co-polar 355 nm total attenuated backscatter $\beta^{\text{att}}_{\text{tot}}$. The MLE is based on optimal estimation with physically constrained minimization (Ehlers et al., 2022) and selecting the optical properties that agree the most with a pre-defined physical state of the atmosphere, i.e. positive optical depth and LR bounded between 2 sr and 200 sr. It comes with particulate extinction α_{part} and co-polar backscatter β_{part}, lidar ratio LR, scattering ratio SR and local optical depth LOD given at coarser resolution of $\approx$ 90 km and referred as observation. The present study uses the MLE product given at sub-observation level of $\approx$ 18 km horizontal (i.e. then corresponding to 3 consecutive SCA measurements for the period 13 December 2021 to 04 April 2022). It is referred as the MLEsub. More details about the SCA and MLE algorithms can be found in the Level 2A Algorithm Theoretical Basis Document (ATBD) (Flamant et al., 2022). The L2A product labelled Baseline 16 includes ready-to-use quality check (QC) for the MLEsub product. The

https://doi.org/10.5194/egusphere-2026-2575
Preprint. Discussion started: 26 May 2026

QC are based on SNR and error estimates. The MLEsub extinction α_{part} is flagged valid for Rayleigh SNR above 70 and standard deviations of α_{part} below 1.0×10^{-2} m^{-1}. The MLEsub backscatter β_{part} is flagged valid for Mie SNR above 30 and standard deviations of β_{part} below 1.0×10^{-3} $\text{m}^{-1}\text{sr}^{-1}$. They have been gradually fine tuned by the Aeolus Data, Innovation, and Science Cluster (DISC) using sensitivity test, and are designed to be restrictive. They discard up to 40 $\%$ of the profiles, especially in low signal conditions below aerosol layers or close to the surface (Trapon et al., 2025). The validity checks are fully described and illustrated in the Level 2A User Guide (Trapon et al., 2022). The present study applies these QC differently depending on the used case. They are not applied when focusing on single overpasses crossed with reference measurements by other lidars (i.e. section 3.1) and when using weekly global map (i.e. section 3.2.1). This allows to keep as many valid bins as possible for the cross validation with referenced measurement, and to make the identification of the aerosol global distribution with global map easier. But they are applied with two-dimensional histograms of L2A extinction versus backscatter (i.e. section 3.2.1, Appendix A2.2) as the objective is to provide qualitative statistics from quality assured product. Additionally, 2 thresholds are applied for the global map and the two-dimensional histograms: the particles-free regions of the atmosphere are discarded removing the bins where MLEsub SR <= 2, and the bins where MLEsub LR get too close to the lower limit of 2 sr and upper limit of $\approx$ 200 sr are discarded (i.e. removal of bins where LR <= 3 sr and where LR >= 199 sr, assuming a non-perfect minimization). The ready-to-use L2A cloud screening (see details in Appendix A1.4) is applied for every conditions.

2.2 Aeolus range bin settings and Tonga specific band

The Aeolus vertical profiling correspond to 24 range bins for which the thickness can be adjusted. Multiple Range Bin Settings (RBS) can be defined at the same time per orbit, for Rayleigh and Mie separately (ESA). This allowed to quickly set specific RBS during Near-Real-Time operation for specific areas of interest within geographical boxes, e.g. increasing the resolution in the troposphere above Cabo Verde to further study the Saharan Air Layer or extending the top height to observe the disruption of the quasi-biennial oscillation (QBO) (Reitebuch et al., 2024). Aeolus upper limit was limited to a maximum of 30 km because of practical signal detection for reliable wind data with primary Rayleigh measurements, the laser signal strength and SNR becoming too low in upper atmosphere. Such RBS adjustment was achieved on 24 January 2022 at 00:00:00 UTC, i.e. moving the top bin measurement to the maximum of 30 km height (i.e. including both Rayleigh and Mie channel) for all longitudes in a latitude band [35° S–0° N] (see Fig. 1, dotted red) referred as Tonga band, and setting the 24 range bin thickness to 1.25 km up to 28 km height and 1 km above. The objective was to capture the Hunga stratospheric aerosols during their descent in altitude. These settings have been extended to the band [35° S–10° N] (see Fig. 1, solid red) on 31 January 2022 at 00:00:00 UTC. The present study uses these two settings of the Tonga band. An update has been done on 14 March 2022 at 00:01:00 UTC following routine monitoring of the plume altitude. The top height bin was set to 26 km altitude and the following settings have been applied for the band [35° S–10° N]: 1 km thickness below 13.5 km altitude, 1.25 km thickness between 13.5 km and 21 km altitude, and 1.5 km thickness above. On 02 May 2022 at 00:22:09 UTC these settings have been extended to the band [35° S–20° N] until 19 March 2023. These final settings are not used in the present study, but offer the opportunity to study the long term impact of the Hunga aerosols.

https://doi.org/10.5194/egusphere-2026-2575
Preprint. Discussion started: 26 May 2026

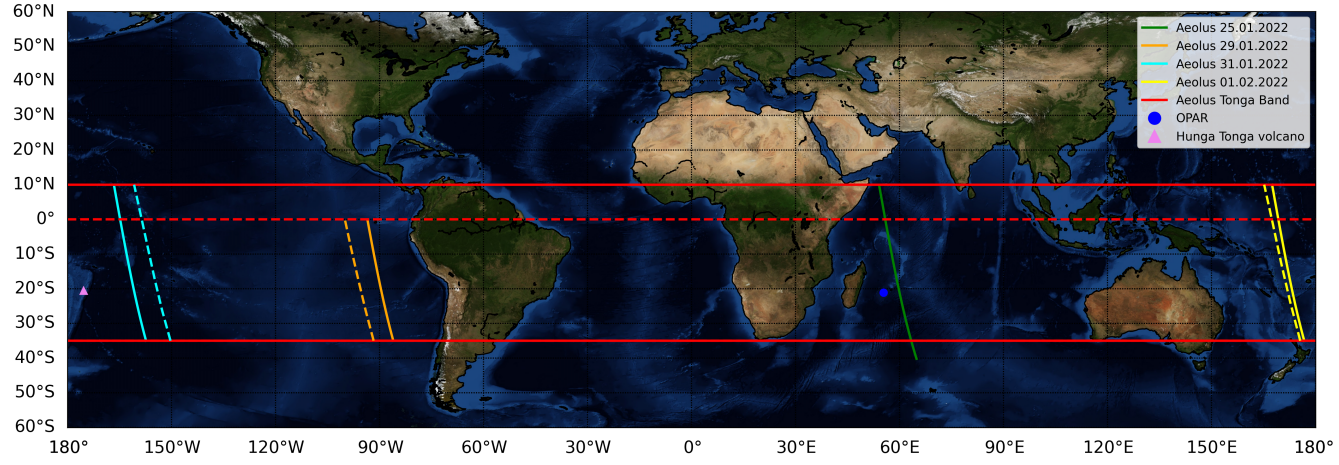

Figure 1. Aeolus Tonga latitudes band (i.e. red) and ground tracks of Aeolus ascending overpasses on 29 January 2022 (i.e. orange, from 00:08:32 UTC to 00:17:26 UTC), 31 January 2022 (i.e. cyan, from 04:53:48 UTC to 05:05:13 UTC) and 01 February 2022 (i.e. yellow, from 06:37:22 UTC to 06:48:26 UTC). The ground tracks of CALIOP closest overpasses with ascending orbit for 29 January 2022 (i.e. orange, from 21:07:32 UTC to 21:17:12 UTC), 31 January 2022 (i.e. cyan, from 01:02:09 UTC to 01:14:33 UTC) and 01 February 2022 (i.e. yellow, 03:18:15 UTC to 03:30:39 UTC) are shown with dotted lines. The blue Marble collection is used for background map (courtesy: https://visibleearth.nasa.gov/, last access: 02 February 2026). The locations of OPAR (i.e. blue) and Hunga Tonga volcano (i.e. rose) are overimposed over the background map.

3 Results

3.1 Aeolus early detection of the Hunga aerosols in late January 2022

3.1.1 Cross validation with ground-based lidars

125 The early evolution of the aerosol plume has been successfully observed with facility 4 days after the eruption (Baron et al., 2023) and several aerosol layers have been captured from 19 January 2022 to 27 January 2022. The layer referred as N6 in Baron et al. (2023) and observed with clear signal maximum at 19.3 km altitude on 25 January 2022 has been selected to be crossed with Aeolus as the ascending overpass comes with limited geolocation offset (i.e. ≈ 705 km). This allows to validate the aerosol optical properties and height from the L2A product with independent measurement.

https://doi.org/10.5194/egusphere-2026-2575
Preprint. Discussion started: 26 May 2026

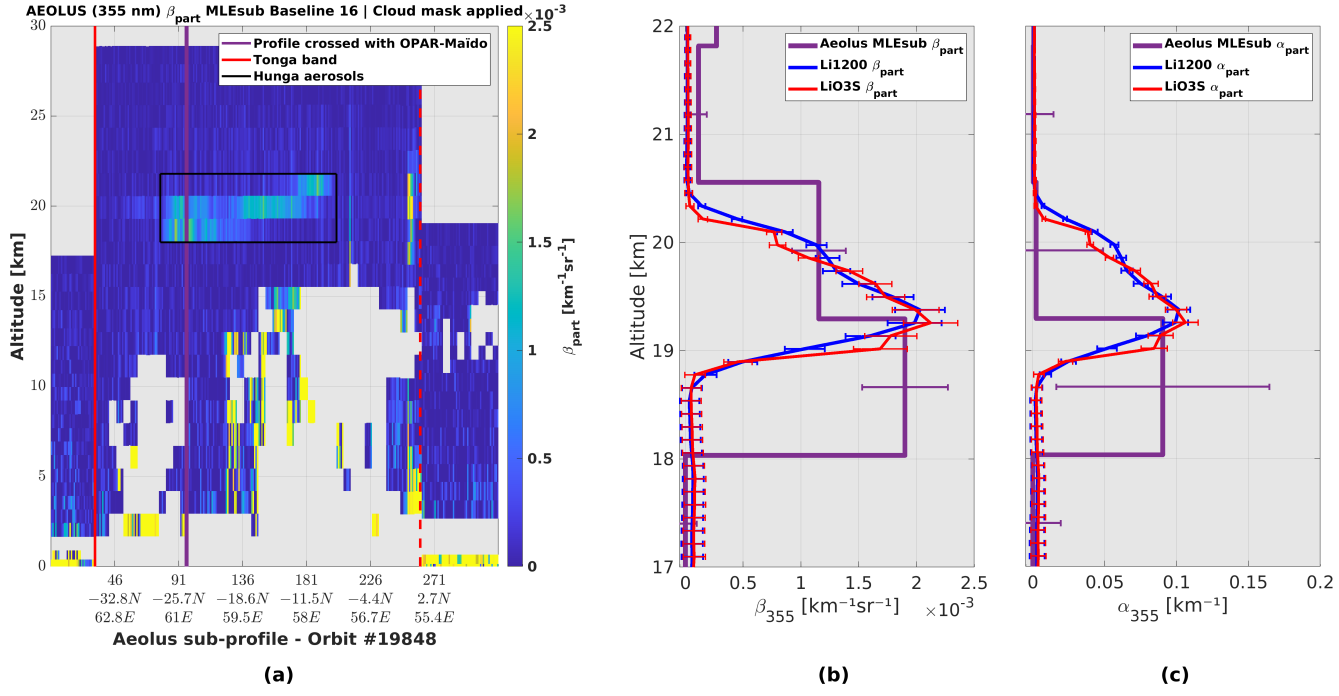

Figure 2. Aeolus cloud screened MLEsub β_{part} on 25 January 2022 (a) and cross of 2D profiles above La Reunion, with LiO3S and Li1200 Klett retrievals for MLEsub β_{part} (b) and MLEsub α_{part} (c) with standard deviations shown as error bars.

Figure 2 shows Aeolus MLEsub 355 nm co-polarized β_{part} for a total of 315 consecutive profiles of $\approx$ 18 km each in the horizontal direction, for ascending section from $\approx$ [-40° N–65° E] to $\approx$ [10° N–54° E]. Ground track of the orbit is shown in Figure 1 (i.e. green). The cloud mask is applied and helps removing dense water clouds observed between 5 km to 15 km altitude. It does not remove a dense layer clearly observable in 3 range bins from $\approx$ 18 km to $\approx$ 20.5 km height between -27° N and -7° N (i.e. Fig 2a, black box), and attributed to the Hunga aerosol layer. Several studies reported high SO_2 concentration with aerosol effective radius $\approx$ 0.2 µm for this layer (Asher et al., 2023; Taha et al., 2022). The cross of Aeolus MLEsub (i.e. Fig. 2b-c, violet) with Li1200 (i.e. Fig. 2b-c, blue) and LiO3S (i.e. Fig. 2b-c, red) for both β_{part} and α_{part} at 355 nm reveal solid agreement. The MLEsub profile 96 (i.e. Fig.2a, violet), which comes with β_{part} of $\approx 2.0 \times 10^{-3}$ km^{-1}sr^{-1} and α_{part} of $\approx$ 0.1 km^{-1} for the range bin from 18 km to 19.25 km with maximum column value SR of 3.2, indeed matches nicely the ground-based retrievals, despite the geolocation offset. The Aeolus profile 96 correspond to day time 14:14:38 UTC and the signal accumulation was done between $\approx$ 02:00 and $\approx$ 15:00 UTC. MLEsub SR , LOD, and LR are equal to 3.2, 0.11, and 47.5 sr respectively for the range bin from 18 km to 19.25 km. The LR value matches the reported estimation of 46 sr by Baron et al. (2023), and derived on same day with the lidars for the in-core layer at 19.3 km in altitude.

https://doi.org/10.5194/egusphere-2026-2575
Preprint. Discussion started: 26 May 2026

3.1.2 Visual comparison with space-borne CALIOP

Figure 3 shows cloud screened $\beta_{\text{tot}}^{\text{att}}$ given at resolution ≈ 6 km horizontal for the active Tonga band (i.e. Fig. 1, red) with top height bin up to 30 km altitude for the dates 29 January 2022, 31 January 2022, and 01 February 2022 (i.e. Fig. 1, solid lines orange, cyan, and yellow respectively). The closest CALIPSO overpass (i.e. Fig. 1, dotted lines orange, cyan and yellow respectively) has been selected for each Aeolus ascending section. Figure 3d-f shows $\beta_{\text{tot,532}}^{\text{att}\parallel}$ for the same Tonga band. Both Aeolus and CALIOP capture well a layer above East Pacific on 29 January 2022 between ≈ 24 km and 28 km in altitude covering a large area from latitudes -20° N to -5° N. The layer appears to be stratified with southern edge located in higher height showing column maximum value SCA $\beta_{\text{tot}}^{\text{att}}$ of $\approx 5.0\times10^{-3}$ km^{-1}sr^{-1} and CALIOP $\beta_{\text{tot,532}}^{\text{att}\parallel}$ of $\approx 3.0\times10^{-3}$ km^{-1}sr^{-1}. On 29 January 2022 the instruments ALADIN and CALIOP captured a layer with elongated northern tale up to the equator and with comparable column maximum value in SCA $\beta_{\text{tot}}^{\text{att}}$ and $\beta_{\text{tot,532}}^{\text{att}\parallel}$ of $\approx 6.0\times10^{-3}$ km^{-1}sr^{-1}. A similar feature is captured on 01 February 2022 above the South West Pacific Ocean (Fig. 4c and Fig. 4f), and transported toward West. High SA concentration have been reported for these plumes above ≈ 24 km altitude because of moister air and active conversion from SO_2 (Zhu et al., 2025). Table 1 summarizes the mean of MLEsub β_{part}, α_{part}, SR, LOD, and LR measured for these layers after applying a conservative MLEsub SR threshold of 5. The column maximum value are indicated in parenthesis and the scores with applied QC flags are indicated in bold. One should note the varying extinction and scattering properties of the layers despite relatively close mean MLEsub β_{part}. If compared to the averaged scores, the plume on 31 January 2022 and 01 February 2022 exhibits high MLEsub column maximum value SR of 37.1 and α_{part} of 317.8 Mm^{-1}. This suggests heterogeneous optical properties as confirmed by the different pattern observed in Fig. 3a-f: the northern elongated tale exhibits higher values in attenuated backscatters. Interestingly, we do observe opposite behavior for the plume observed on 29 January 2022 as the southern and compact branch comes with higher backscatter (i.e. Fig. 3a). It is also important to note the deviation of these optical properties when compared to the early SO_2 plume observed above La Reunion in lower altitudes.

https://doi.org/10.5194/egusphere-2026-2575
Preprint. Discussion started: 26 May 2026

Scores for MLEsub SR >5	β_{part} [$\text{Mm}^{-1}\text{sr}^{-1}$]	α_{part} [Mm^{-1}]	SR []	LOD []	LR [sr]
29.01.2022	2.6 (6.8)	75.8 (317.8)	13.4 (37.1)	0.1 (0.4)	34.8 (143.4)
	2.6 (6.8)	**96 (317.8)**	-	-	**31.2 (135.1)**
31.01.2022	2.6 (6.5)	60.7 (232.3)	10 (21.9)	0.07 (0.3)	22.3 (126.9)
	2.6 (6.5)	**60.7 (232.3)**	-	-	**22.3 (126.9)**
01.02.2022	2.2 (4.5)	33.6 (157.2)	8.4 (15.6)	0.04 (0.3)	15.1 (106.1)
	2.2 (4.5)	**33.6 (157.2)**	-	-	**15.1 (106.1)**

Table 1. Summary of the statistics of the mean and maximum values for the stratospheric plumes' optical properties retrieved from Aeolus MLEsub. The maximum values are indicated in parenthesis. The scores with applied QC are indicated in bold.

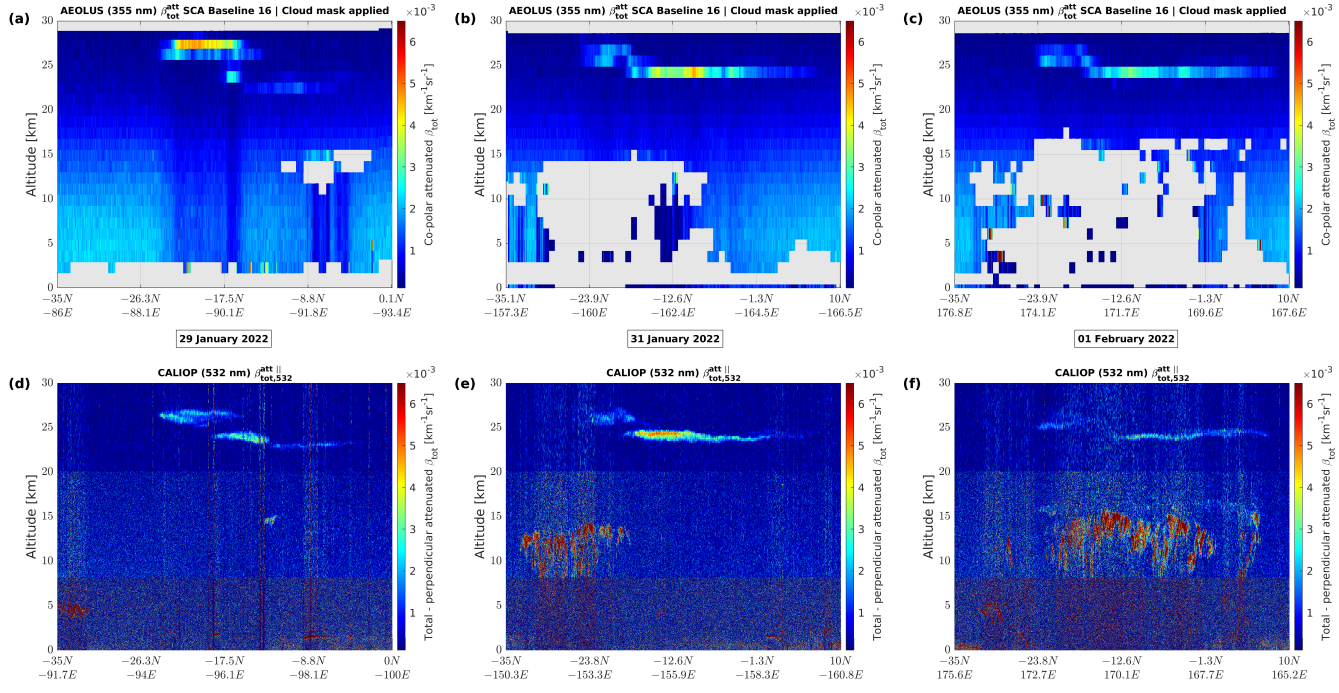

Figure 3. Aeolus cloud screened SCA $\beta^{\text{att}}_{\text{tot}}$ sections in the Tonga band on 29 January 2022, 31 January 2022 and 01 February 2022 (a-c), and CALIOP $\beta^{\text{att}||}_{\text{tot,532}}$ closest sections on same days (d-f).

3.2 Spatio-temporal evolution of the Hunga optical properties until March 2022

3.2.1 Aerosol global distribution two weeks after the eruption

Aeolus featured a 7-days orbital repeat cycle to achieve a full global coverage of the Earth. The satellite completed ≈ 15 orbits per day and ≈ 105 orbits per week for the entire mission lifetime, returning to the same ground track every week to ensure

https://doi.org/10.5194/egusphere-2026-2575
Preprint. Discussion started: 26 May 2026

consistent global wind and aerosols measurements. This weekly cycle offers the opportunity to have a detailed view of the global Hunga aerosol distribution over time. The present study proceeds with 6 consecutive weekly datasets of Aeolus L2A product and using the optical properties derived from the MLEsub. It covers the period from 24 January 2022 00:00:00 UTC to 06 March 2022 00:00:00 UTC, focusing on the active Tonga band (i.e. [35° S–0° N] for the first week until 31 January 2022, and [35° S–10° N] afterwards). This allows to keep RBS consistency with maximum height measurement up to 30 km altitude. Global map are derived from the L2A product as following: for every vertical profile, and only above 18 km altitude, the range bin with column maximum value of MLEsub SR is determined as indicator of the centre of mass of the Hunga aerosol plume. The aerosol retrievals measured for these very range bins, e.g. β_{part}, α_{part}, and SR are then assigned for each profile of $\approx$ 18 km horizontal, and represented with a dot on worldmap. Figure 4a shows the global map of the column maximum value SR for the first week from 24 January 2022 00:00:00 UTC to 30 January 2022 00:00:00 UTC over all longitudes. The particles-free regions with SR below 2 appear as white. Figure 4b shows the height, i.e. upper limit of the range bin, where the column maximum value SR has been identified. The quality assured IMS SA OD and IMS SO_2 product for both daytime and nighttime swaths are averaged for the same period. Each weekly average map then correspond to the arithmetic mean of 14 swaths. They are shown respectively with Fig. 4c and Fig. 4d. Several observations can be made and are summarized as follows:

1. The valid Aeolus maximum column values SR above 18 km and pointing to the Hunga in-core plume mainly appear in latitude [-30° N– -10° N] and longitudes [70° E–160° W]. Three main branches with specific SR order of magnitudes can be observed: a southern branch with SR values above 8 (i.e. Fig. 4a, red box), a northern West branch with SR between 5 to 8 (i.e. Fig. 4a, violet boxes), and localized northern East branch with lower SR below 5 (i.e. Fig. 4a, blue boxes).

2. The three branches occupy differentaltitudes, i.e. the northern East branch showing lower altitudes $\approx$ 18 km to 22 km (i.e. Fig. 4b, blue boxes) than the southern branch with $\approx$ 26 to 28 km (i.e. Fig. 4b, red box). The northern branch matches $\approx$ 24 to 26 km (i.e. Fig. 4b, violet boxes).

3. The southern branch matches nicely the high values of IMS SA OD up to 0.025 (Fig. 4c, light orange to red), revealing compact SA patches for longitudes [90° W–60° E].

4. The IMS SO_2 map shows dominant blue color code for the these SA patches (i.e. Fig. 4d), then confirming a low concentration of SO_2 and suggesting a conversion to sulfate that has already been completed.

5. The IMS SO_2 map reveals higher SO_2 concentration up to $\approx$ 2.0 ppbv (Fig. 4d, light green to orange) for the northern East branch which exhibits lower MLEsub SR and matches lower altitudes $\approx$ 18 to 22 km. This corroborates the observations made at La Reunion on 25 January 2022 in Fig. 1 where the in-core plume shows column maximum value SR, β_{part} and α_{part} at $\approx$ 19.3 km altitude.

6. The SO_2 plume appear to be localized in a band [25° S–5° S] and is mainly distributed over south Africa and East Atlantic, confirming the results by Boichu et al. (2023).

https://doi.org/10.5194/egusphere-2026-2575
Preprint. Discussion started: 26 May 2026

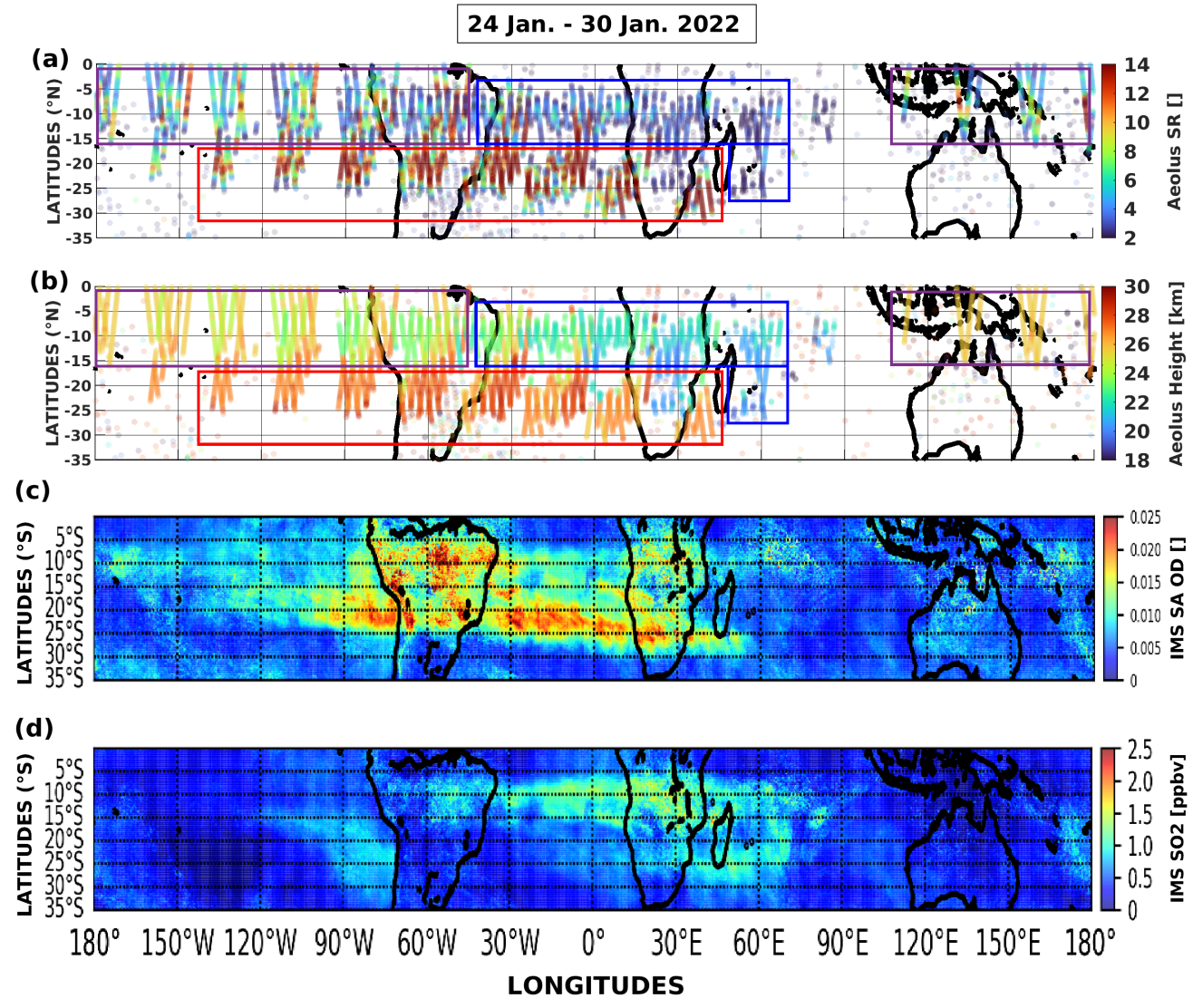

Figure 4. Aeolus weekly global map of column maximum value SR above 18 km altitude (a) and their corresponding height bin (b) for the period 24 January 2022 00:00:00 UTC to 30 January 2022 00:00:00 UTC. The marker size in the (a) and (b) are chosen randomly and do not correspond to their footprint. The weekly average of IMS SA OD and IMS SO_2 for daytime and nighttime swaths are respectively shown in (c) and (d).

For every column maximum value SR shown in Fig. 4a, the corresponding β_{part} and α_{part} measured for the the same range bin are selected. Figure 5 shows a two-dimensional histogram of $\log10(\alpha_{\text{part}})$ versus $\log10(\beta_{\text{part}})$ with height bin shown by varying colours. The LR ranges are indicated with solid lines in diagonals. Three dominant regimes in altitude can be identified: low altitude from $\approx$ 18 km to $\approx$ 22 km (Fig. 5, blue box), mid altitude between $\approx$ 24 km to $\approx$ 26 km (Fig. 5, violet boxes), and

https://doi.org/10.5194/egusphere-2026-2575
Preprint. Discussion started: 26 May 2026

high altitude above 26 km up to ≈ 28 km (Fig. 5, red box). They exhibit respective LR ranges: ≈ 5 sr to ≈ 60 sr for the low altitude regime, wide range from ≈ 5 sr to ≈ 80 sr for the mid altitude regime, and above 100 sr for the high altitude regime. The IMS SA OD and SO_2 concentration are shown with varying colours with similar two-dimensional histograms in Figs. A4a and A5a. They are determined by calculating the minimum geographical distance with the Aeolus profiles, and assuming the Earth being a perfect sphere with radius of 6371 km. Figure A4a points to high IMS SA OD above 0.015 (i.e. light red to yellow) for both the mid altitude and high altitude regime. Both regimes then seem to correspond to SA plumes distributed in different height, as seen with Fig. 4c. Figure A5a points to high IMS SO_2 concentration above 0.8 ppbv (i.e. yellow) for the low altitude regime below ≈ 22 km.

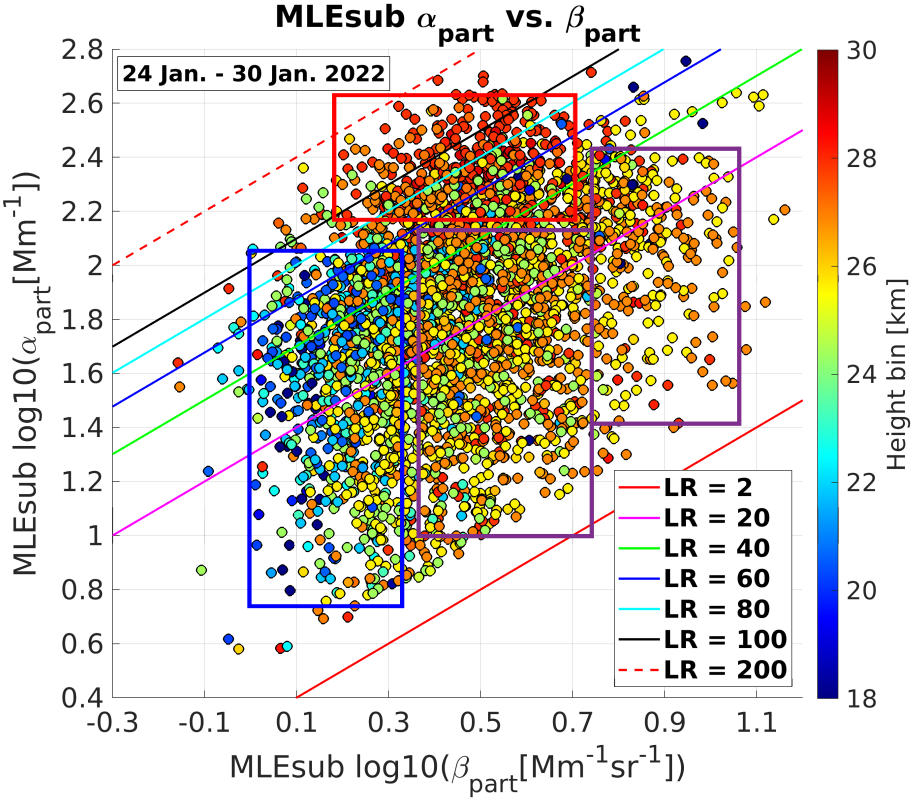

Figure 5. Two-dimensional histograms of Aeolus L2A α_{part} versus β_{part} for every range bin where the column maximum value SR is detected. The L2A QC, cloud mask, and SR threshold of 2 are applied. The panel corresponds to the week for the period 24 January 2022 to 30 January 2022. The height bin are shown by varying colours.

3.2.2 Long-range transport of aging plumes

The weekly map of Aeolus, indicating the centre of mass of the Hunga aerosols with maximum column value SR, and presented in Fig. 4a covers the week from 24 January 2022 to 30 January 2022. It can be reproduced for the 6 consecutive weeks from 24

https://doi.org/10.5194/egusphere-2026-2575
Preprint. Discussion started: 26 May 2026

January 2022 to 06 March 2022 (see Fig. 6a-f). Similarly, the corresponding height bin and LOD are shown with Figs. 7a-f, 8a-f. The weekly average of IMS SA OD and IMS SO_2 can also be reproduced until 06 March 2022 (see Figs. A1a-f, A2a-f). Finally, the two-dimensional histograms of log10(α_{part}) versus log10(β_{part}) measured by Aeolus for each week are presented with Fig. A3a-f (height bin shown by varying colours), Fig. A4a-f (IMS SA OD shown by varying colours), and Fig. A5a-f (IMS SO_2 concentration shown by varying colours). This offers the opportunity to track the SA and SO_2 plumes previously identified during their zonal and meridional transport, and to assess the evolution of their height and optical properties over time. Figure A1a-f then show the southern SA patches observed in late January 2022 above $\approx$ 26 km in altitude up to $\approx$ 28 km: the compact patches with higher SA OD above 0.015 (i.e. orange to red) appear to quickly drift West and South (Fig. A1a-c), completing a full Earth circumnavigation by mid February (i.e. Figs. A1b, A1d). They quickly stabilize in lower height between $\approx$ 25 and 27 km in altitude (Fig. 7a-f, light orange and Fig. 8a-f, red) in latitudes [25° S– 15° S], and appear to stay at this in altitude until 06 March 2022. A two branches separation can be seen by mid February 2022 and Figure 7a-f shows a clear vertical distribution between the southern and compact SA patches and northern elongated tales that disperse between $\approx$ 23 and 25 km in altitude (i.e. light green) up to the equator in latitudes [15° S– 10° N]. FigureA2a-f confirms a quick disaggregation of the SO_2 plume by mid February 2022, corroborating the results by Carn et al. (2025) and Sellitto et al. (2024b), and it's trace in Fig. 7a-c (i.e. light blue) with in altitude below $\approx$ 22 km in altitude indeed disappears, showing a short stratospheric lifetime. Interestingly, the southern SA patches comes with the highest α_{part} (Fig. A3a-f, red) and LOD (Fig. 8a-f, red), and retain high UV scattering properties with SR above 8 until 06 March 2022 (Fig. 6a-f, light blue to orange). Figures A3, A4, A5 show the evolution of the 3 dominant regimes identified in Fig. 5 (i.e. dominant blue associated to the SO_2 plume below 22 km in altitude, dominant red associated to SA compact patches above 25 km in altitude, and dominant yellow to green associated to SA residuals between 23 to 25 km in altitude). The red regime of LR values above 100 sr and high α_{part} above 150 Mm^{-1} points to the leading edges of the SA compact patches above $\approx$ 27 km in altitude and cannot be observed by February 2022 (i.e. Fig. A3b). The yellow to green regime of SA residuals exhibits lower α_{part} below 100 Mm^{-1}, and lower LR below $\approx$ 80 sr which converge below $\approx$ 60 sr over time. Figure 8a-f shows how the LOD of the southern SA patches rapidly stabilize below 0.04 (Fig. 8a-f, red). These decreasing trends of the SA LR and LOD over time are in line with findings by Duchamp et al. (2026). Moreover, the LR lower values point to coarse mode and suggest that after a quick increase in size, the high sedimentation rate of the SA plume is stabilizing over time as they stay at altitudes between $\approx$ 24 to 26 km during the long-range transport with relatively stable optical properties. This agrees with the aerosol effective radius derived from solar occultation with Stratospheric Aerosol and Gas Experiment III (SAGE III) on board the International Space Station (ISS) and reported in Khaykin and Bourassa (2025): two peaks of $\approx$ 0.3–0.4 nm can be respectively observed at distinct altitudes $\approx$ 24 and $\approx$ 26 km by February 2022.

https://doi.org/10.5194/egusphere-2026-2575
Preprint. Discussion started: 26 May 2026

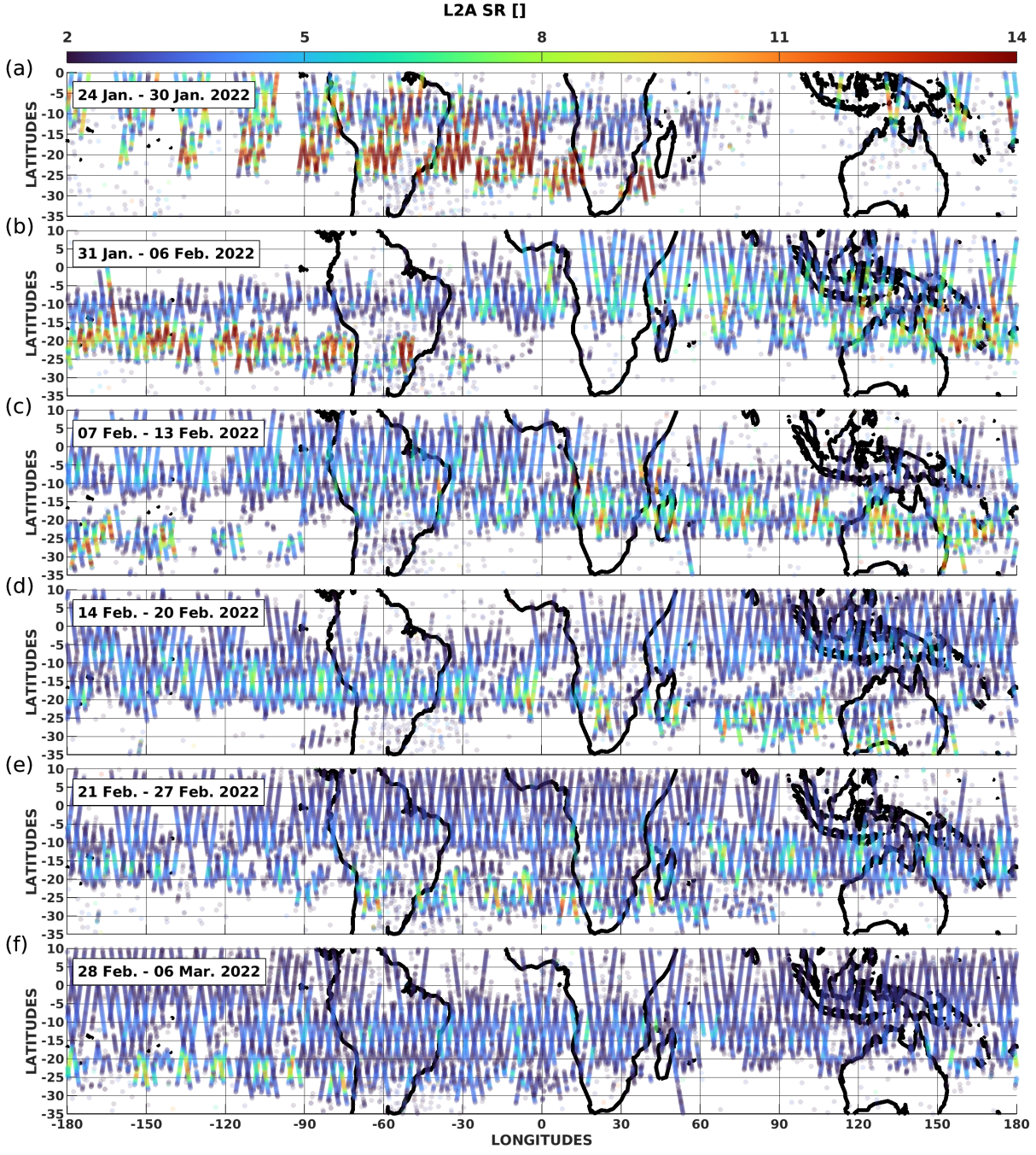

Figure 6. Aeolus weekly global map of column maximum value SR above 18 km altitude (a-f). The marker size are chosen randomly and do not correspond to their footprint. The L2A cloud mask and the MLEsub SR threshold of 2 are applied.

https://doi.org/10.5194/egusphere-2026-2575
Preprint. Discussion started: 26 May 2026

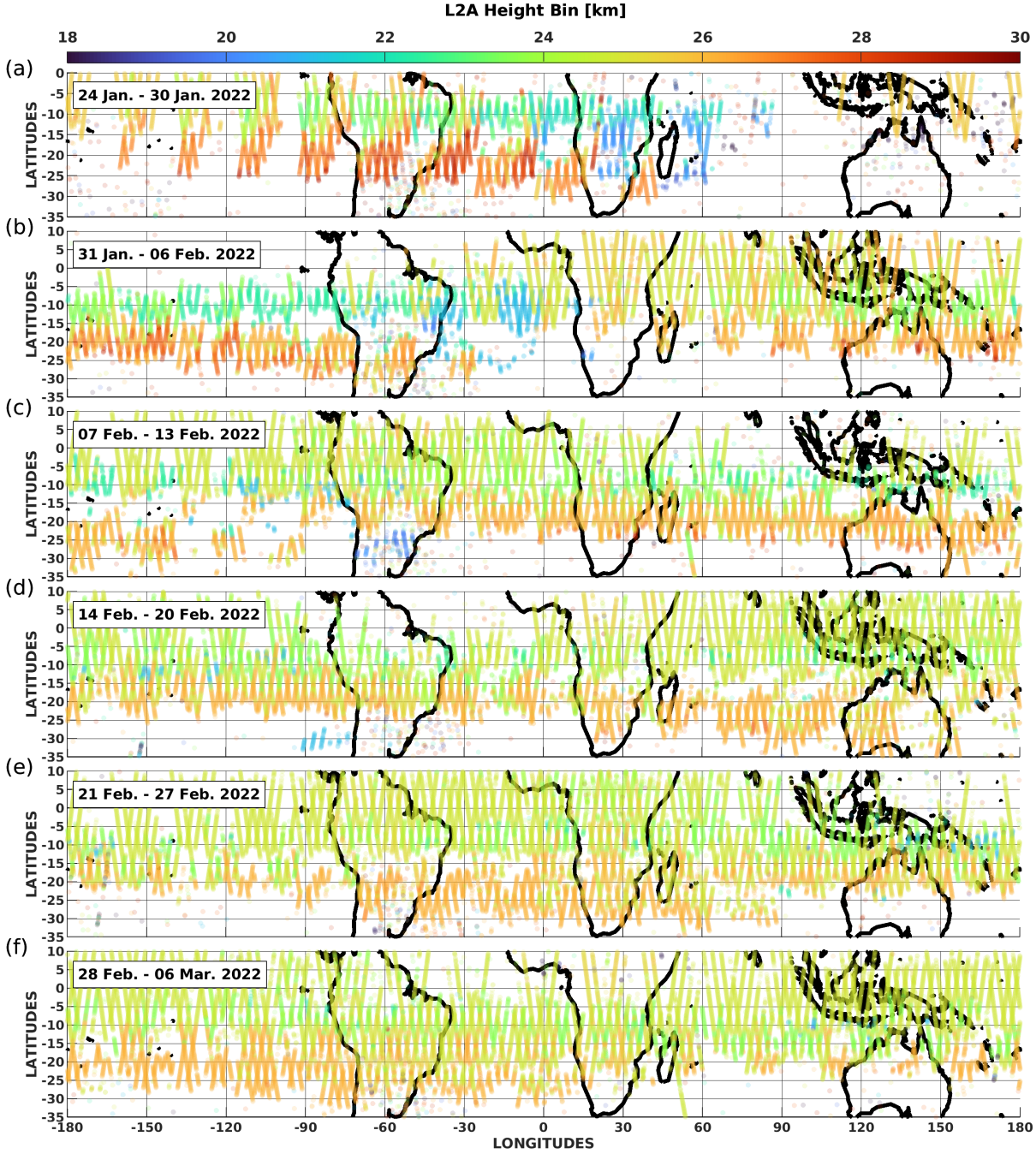

Figure 7. Aeolus weekly global map of height for the range bin with column maximum value SR above 18 km altitude (a-f). The marker size are chosen randomly and do not correspond to their footprint. The L2A cloud mask and the MLEsub SR threshold of 2 are applied.

https://doi.org/10.5194/egusphere-2026-2575
Preprint. Discussion started: 26 May 2026

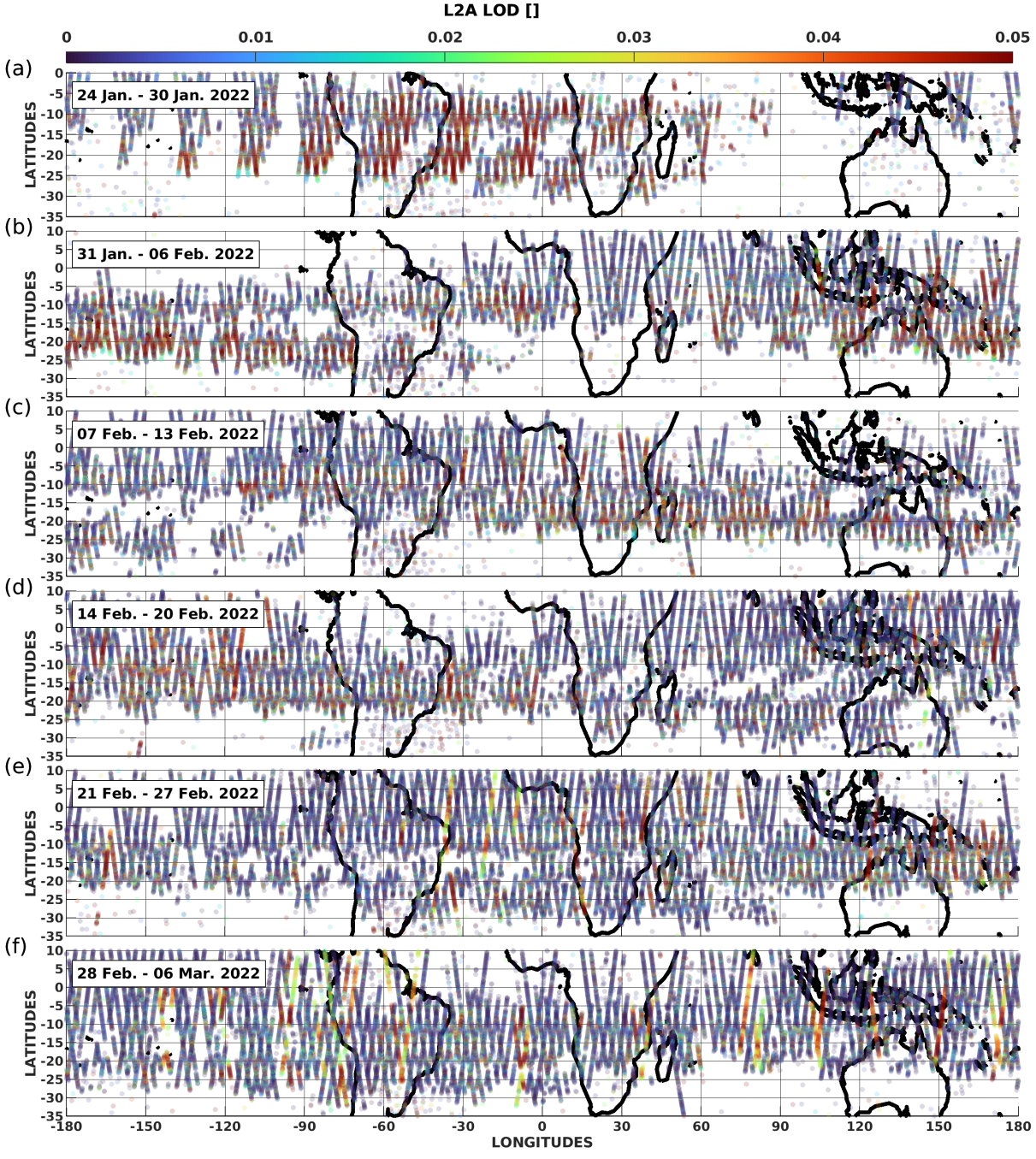

Figure 8. Aeolus weekly global map of LOD for the range bin with column maximum value SR above 18 km altitude (a-f). The marker size are chosen randomly and do not correspond to their footprint. The L2A cloud mask and the MLEsub SR threshold of 2 are applied.

https://doi.org/10.5194/egusphere-2026-2575
Preprint. Discussion started: 26 May 2026

4 Discussions and conclusion

The study highlights observations of the Hunga 2022 stratospheric aerosols by the ALADIN instrument, the first UV Wind Doppler lidar with HSR capacity in space, on board the Aeolus satellite and using the L2A product derived with the SCA and MLEsub algorithms. Orbit sections intersecting the Hunga plumes in the southern equatorial region [35 °S–10° N] on late January 2022 are selected, and the independent measurement of backscatter and extinction coefficients for particles are compared with reference atmospheric lidars. Several Hunga plumes are observed: the cross-comparison of MLEsub profiles of ≈ 18 km horizontal with ground-based lidars Li1200 and LiO3S at La Reunion on 25 January 2022 reveals a plume between ≈ 18 and ≈ 21 km in altitude in latitudes [26 °S– 5 °S]. The extinction-to-backscatter LR of 47.5 sr measured by Aeolus for the centre of mass of the Hunga plume, i.e. the most optically thick region identified with maximum column value SR of 3.1, agrees well with the reference lidars. Other plumes are observed until 01 February 2022 above the Pacific Ocean and at higher in altitude ≈ 25 km to 28 km: both CALIOP on board the CALIPSO satellite and ALADIN onbaord Aeolus capture well optically thick aerosol layers distributed between latitudes [25 °S–0°]. Aeolus measured higher α_{part}, and LR with maximum values of 317.8 Mm^{-1} and 135.1 sr when compared to the plume observed above La Reunion.

The zonal and meridional evolution of these aerosol plumes are shown in the present study until 06 March 2022, valuing the Aeolus coverage and using weekly global map. The map are produced for SR, LOD, and height where the centre of mass of the plume is detected. They are analysed for the first time in parallel with weekly average of sulfate-specific OD and SO_2 concentration derived with the RAL/IMS scheme from collocated instruments IASI, AMSU and MHS on board Eumetsat MetopB spacecraft. The map reveal a short-lived plume with low IMS SA OD and high IMS SO_2 concentration above south Africa in latitudes [25 °S – 10 °S] in late January 2022. Aeolus measures SR and LR below 5 and 60 sr respectively, with height of ≈ 18 to 22 km. For the same period, the global map show SA plumes in higher altitudes from ≈ 24 km to 28 km in altitude, mainly distributed in latitudes [30 °S – 15 °S]. It is composed of optically thick and compact SA patches with IMS SA OD up to 0.025, and low IMS SO_2 concentration below 1.0 ppbv then assuming a conversion from SO_2 to sulfate that has been completed almost entirely. The SA long-lived patches are observed drifting south and transported west, circumnavigating the Earth every two weeks. During their rapid transport westward ($\approx 50°$ longitude per week) and southward ($\approx 5°$ latitude per week until late February 2022), they retain characteristic optical properties: strong UV signal extinction up to ≈ 350 Mm^{-1} and SR up to 40, and high LR above 100 sr. The most optically thick plume appears to stay compact and stabilize at high altitude ≈ 25 to 27 km in latitudes [30° S–15° S] with LR below 80 sr. Interestingly, part of the plume also disperse as far as the equator at lower altitude of ≈ 23 to 25 km and spread over large areas in latitudes [15° S–10° N], reaching more modest SR below 8 and LR below 60 sr.

The sulfate plume sedimentation was assumed to be more pronounced on certain latitudes in previous studies (Legras et al., 2022)). The present study confirms this hypothesis showing lower height of SA patches that disperse in the northern branch [15° S–10° N] with higher sedimentation rate. The fast transport of the Hunga aerosols towards the southern pole (Khaykin et al., 2022; Kloss et al., 2025) and the plume two branches separation by February 2022 (Sellitto et al., 2022), date on which the SO_2 signal is not observable contrary to SA (Sellitto et al., 2024b), can also be confirmed. Additionally, the vertical

https://doi.org/10.5194/egusphere-2026-2575
Preprint. Discussion started: 26 May 2026

gradient of UV LR measured by Aeolus is an important findings. It suggests unequal microphysical properties of the sulfate particles that compose the main Hunga plumes, the higher LR values above 100 sr in the early top filament up to $\approx$ 28 km in altitude pointing to fine mode. The top edge plume is characterized by strong UV absorption (i.e. α_{part} up to 350 Mm^{-1}, LOD above 0.2) and scattering (i.e. β_{part} up to 6.0 $\mathrm{Mm}^{-1}.\mathrm{sr}^{-1}$, SR up to 40) capacities. This is consistent with the reported unusual characteristics and particles size distribution for the Hunga early plumes (Asher et al., 2023; Duchamp et al., 2026). The decrease around lower values (e.g. LR below 60 sr, LOD below 0.04, SR below 8) with lower height around $\approx$ 24 km to 26 km in altitude also argue in favor of a stabilization of the merging and growth processes of the sulfate aerosol particles as suggested in Zhu et al. (2025). The study then supports the hypothesis that oxidation of SO_2 to sulfuric acid (H_2SO_4), that may nucleate to sub-micron sulfate aerosols (Kremser et al., 2016), was more pronounced in the plumes top edge above $\approx$ 26 km in altitude. Interestingly, the low altitude plume around $\approx$ 18 km to 22 km corresponding to high IMS SO_2 and low IMS SA concentrations exhibits significantly less strong UV scattering properties (i.e. β_{part} below to 2.0 $\mathrm{Mm}^{-1}.\mathrm{sr}^{-1}$, SR below 5). The role of water vapour in the different plumes could be analysed further as it influences the oxidation of SO_2 as shown by Bruckert et al. (2025). Moreover, hypothesis regarding the atmospheric conditions can be put forward: constant easterly winds depending on latitudes and altitudes affect the dispersion of the different plumes. The Aeolus Level 2B wind product (de Kloe et al., 2023; Rennie et al., 2020) can be used to study the zonal winds and their evolution over time. The Hunga case study highlights how valuable spaceborne atmospheric UV lidars are when observing sub-micron aerosols in the poorly known equatorward stratosphere, with overall good SNR and revisit time. Both horizontal and vertical sampling, and cloud masking, are important points for new missions such as EarthCARE (Illingworth et al., 2015) and Aeolus-2 (Berceau et al., 2025) as they affect the identification of the centre of mass of the plumes, as seen with aerosols from the Ruang eruption (Khaykin et al., 2026).

Data availability. The study includes Aeolus L2A aerosol products prepared by the Aeolus Aeolus Data Innovation and Science Cluster (DISC) (involving ESA, DLR, DoRIT until 2025, ECMWF, KNMI, CNRS until 2022, TROPOS, S&T, ABB, and Serco) and the Payload Data Ground Segment (PDGS) through the reprocessing activities. The corresponding dataset of 2022 is part of the fourth reprocessing, labelled Baseline 16 and covering October 2018 to April 2023. The Aeolus L2A products are available through the ESA MAAP explorer at https://explorer.maap.eo.esa.int/ within the collection « Aeolus L2A Products ». The data of Li1200 (https://doi.org/10.25326/714) and LiO3S (https://doi.org/10.25326/713) are available at the National data and services centre for atmosphere AERIS at https://www.aeris-data.fr. The RAL (Rutherford Appleton Laboratory) Infrared/Microwave Sounder (IMS) data are available at https://doi.org/10.5281/zenodo.7102472 (Siddans and Legras, 2022) (last access:25 January 2026). CALIOP data V4.51 are available at https://asdc.larc.nasa.gov/project/CALIPSO/CAL_LID_L1-Standard-V4-51_V4-51 (NASA/LARC/SD/ASDC) (last access:10 October 2025).

Author contributions. DT is responsible of the maintenance and improvement of the L2A prototype processor for SCA and MLE algorithms. DT conceptualized the study, and scientific discussions have been conducted with the help of SK. HB, SB and AA reviewed internally the paper and also took part in the scientific discussions. MR is responsible of the maintenance and improvement of the Level 2B processor for

https://doi.org/10.5194/egusphere-2026-2575
Preprint. Discussion started: 26 May 2026

wind product, and has contributed to the implementation of the cloud screening in the L2A product. MS is the principal investigation and technical point of contact for the data associated with the observatory and supported both the download and processing of Li1200 and LiO3S retrievals. The paper was written by DT.

Competing interests. The contact author has declared that none of the authors has any competing interest.

Acknowledgements. We thank all previous contributors to the Aeolus L2A product development and validation, including Adrien Lacour (Magellium, formerly CNRM Météo-France) for the preliminary testing of L2A MLEsub with the Hunga case (Lacour et al., 2022). We acknowledge the Aeolus DISC for the complete and successful processing of Aeolus L2A product labelled Baseline 16. We acknowledge all contributors to the online archive « RAL IMS retrieval of SO_2 and sulphates (January to April 2022) ».The study was conducted in the frame of ESA Aeolus DISC Phase F1 subcontract No. D/553/67342749 To ESA contract No. 4000144330/24/I-AG as part of L2A processor version 16 scientific application. This work was partly funded by the European Union under grant agreement No 101086690 and by the COST Action EARLICOST (CA24135), supported by COST (European Cooperation in Science and Technology). The authors acknowledge the support of the ANR through the OBS4CLIM project (ANR-21-ESRE-0013), and CNES through the project EarthCARE.

https://doi.org/10.5194/egusphere-2026-2575
Preprint. Discussion started: 26 May 2026

References

Asher, E., Todt, M., Rosenlof, K., Thornberry, T., Gao, R.-S., Taha, G., Walter, P., Alvarez, S., Flynn, J., Davis, S. M., Evan, S., Brioude, J., Metzger, J.-M., Hurst, D. F., Hall, E., and Xiong, K.: Unexpectedly rapid aerosol formation in the Hunga Tonga plume, Proceedings of the National Academy of Sciences, 120, e2219547 120, https://doi.org/10.1073/pnas.2219547120, 2023.

Baron, A., Chazette, P., Khaykin, S., Payen, G., Marquestaut, N., Bègue, N., and Duflot, V.: Early Evolution of the Stratospheric Aerosol Plume Following the 2022 Hunga Tonga-Hunga Ha'apai Eruption: Lidar Observations From Reunion (21°S, 55°E), Geophysical Research Letters, 50, e2022GL101 751, https://doi.org/https://doi.org/10.1029/2022GL101751, e2022GL101751 2022GL101751, 2023.

Berceau, P., Albano, C., Ballester, M., Belhadj, T., Bellouard, R., Bon, D., Boyes, B., Brouard, L., Krisna, T. C., Chaumeil, F., Ciapponi, A., Corselle, B., Debonne, C., Villèle, G. D., Heliere, A., Marchais, D., Olivier, M., Parzianello, G., Porciani, M., Vétel, C., Wernham, D., and Zimmermann, S.: Aeolus-2 instrument: the new Doppler wind LIDAR, in: International Conference on Space Optics — ICSO 2024, edited by Bernard, F., Karafolas, N., Kubik, P., and Minoglou, K., vol. 13699, p. 136990W, International Society for Optics and Photonics, SPIE, https://doi.org/10.1117/12.3072768, 2025.

Boichu, M., Grandin, R., Blarel, L., Torres, B., Derimian, Y., Goloub, P., Brogniez, C., Chiapello, I., Dubovik, O., Mathurin, T., Pascal, N., Patou, M., and Riedi, J.: Growth and Global Persistence of Stratospheric Sulfate Aerosols From the 2022 Hunga Tonga–Hunga Ha'apai Volcanic Eruption, Journal of Geophysical Research: Atmospheres, 128, e2023JD039 010, https://doi.org/https://doi.org/10.1029/2023JD039010, e2023JD039010 2023JD039010, 2023.

Bruckert, J., Chopra, S., Siddans, R., Wedler, C., and Hoshyaripour, G. A.: Aerosol dynamic processes in the Hunga plume in January 2022: does water vapor accelerate aerosol aging?, Atmospheric Chemistry and Physics, 25, 9859–9884, https://doi.org/10.5194/acp-25-9859-2025, 2025.

Carn, S. A., Krotkov, N. A., Fisher, B. L., and Li, C.: Out of the blue: Volcanic SO2 emissions during the 2021–2022 eruptions of Hunga Tonga—Hunga Ha'apai (Tonga), Frontiers in Earth Science, 10, 962–976, https://doi.org/10.3389/feart.2022.976962, 2025.

Clerbaux, C., Boynard, A., Clarisse, L., George, M., Hadji-Lazaro, J., Herbin, H., Hurtmans, D., Pommier, M., Razavi, A., Turquety, S., Wespes, C., and Coheur, P.-F.: Monitoring of atmospheric composition using the thermal infrared IASI/MetOp sounder, Atmospheric Chemistry and Physics, 9, 6041–6054, https://doi.org/10.5194/acp-9-6041-2009, 2009.

Dabas, A., Denneulin, M.-L., Flamant, P., Loth, C., Garnier, A., and Dolfi-Bouteyre, A.: Correcting winds measured with a Rayleigh Doppler lidar from pressure and temperature effects, Tellus A: Dynamic Meteorology and Oceanography, 60, 206–215, https://doi.org/10.1111/j.1600-0870.2007.00284.x, 2008.

de Kloe, J., Stoffelen, A., Tan, D., Andersson, E., Rennie, M., Dabas, A., Poli, P., and Huber, D.: ADM-Aeolus Level-2B/2C Processor Input/Output Data Definitions Interface Control Document, Tech. rep., ESA, https://earth.esa.int/eogateway/documents/20142/37627/Aeolus-L2B-2C-Input-Output-DD-ICD.pdf, version 3.90 (last access: 20 May 2023), 2023.

Duchamp, C., Legras, B., Podglajen, A., Sellitto, P., Bourassa, A. E., Rozanov, A., Taha, G., and Zawada, D. J.: Aerosol Composition and Extinction of the 2022 Hunga Plume Using CALIOP, Atmospheric Measurement Techniques, 19, 1675–1696, https://doi.org/10.5194/amt-19-1675-2026, 2026.

Duflot, V., Baray, J.-L., Payen, G., Marquestaut, N., Posny, F., Metzger, J.-M., Langerock, B., Vigouroux, C., Hadji-Lazaro, J., Portafaix, T., De Mazière, M., Coheur, P.-F., Clerbaux, C., and Cammas, J.-P.: Tropospheric ozone profiles by DIAL at Maïdo Observatory (Reunion Island): system description, instrumental performance and result comparison with ozone external data set, Atmospheric Measurement Techniques, 10, 3359–3373, https://doi.org/10.5194/amt-10-3359-2017, 2017.

https://doi.org/10.5194/egusphere-2026-2575
Preprint. Discussion started: 26 May 2026

Ehlers, F., Flament, T., Dabas, A., Trapon, D., Lacour, A., Baars, H., and Straume-Lindner, A. G.: Optimization of Aeolus' aerosol optical properties by maximum-likelihood estimation, Atmospheric Measurement Techniques, 15, 185–203, https://doi.org/10.5194/amt-15-185-2022, 2022.

ESA: A Guide to Aeolus Range Bin Settings, https://earth.esa.int/eogateway/news/a-guide-to-aeolus-range-bin-settings.

Flamant, P., Cuesta, J., Denneulin, M.-L., Dabas, A., and Huber, D.: ADM-Aeolus retrieval algorithms for aerosol and cloud products, Tellus A: Dynamic Meteorology and Oceanography, 60, 273–286, https://doi.org/10.1111/j.1600-0870.2007.00287.x, 2008.

Flamant, P., Dabas, A., Martinet, P., Lever, V., Flament, T., Trapon, D., Olivier, M., Cuesta, J., and Huber, D.: Aeolus L2A Algorithm Theoretical Baseline Document, Particle optical properties product, Tech. rep., ESA, https://earth.esa.int/eogateway/catalog/aeolus-l2a-aerosol-cloud-optical-product, version 6.0 (last access: 17 January 2025), 2022.

Flament, T., Trapon, D., Lacour, A., Dabas, A., Ehlers, F., and Huber, D.: Aeolus L2A aerosol optical properties product: standard correct algorithm and Mie correct algorithm, Atmospheric Measurement Techniques, 14, 7851–7871, https://doi.org/10.5194/amt-14-7851-2021, 2021.

Floutsi, A. A., Baars, H., Engelmann, R., Althausen, D., Ansmann, A., Bohlmann, S., Heese, B., Hofer, J., Kanitz, T., Haarig, M., Ohneiser, K., Radenz, M., Seifert, P., Skupin, A., Yin, Z., Abdullaev, S. F., Komppula, M., Filioglou, M., Giannakaki, E., Stachlewska, I. S., Janicka, L., Bortoli, D., Marinou, E., Amiridis, V., Gialitaki, A., Mamouri, R.-E., Barja, B., and Wandinger, U.: DeLiAn – a growing collection of depolarization ratio, lidar ratio and Ångström exponent for different aerosol types and mixtures from ground-based lidar observations, Atmospheric Measurement Techniques, 16, 2353–2379, https://doi.org/10.5194/amt-16-2353-2023, 2023.

Gantois, D., Payen, G., Sicard, M., Duflot, V., Bègue, N., Marquestaut, N., Portafaix, T., Godin-Beekmann, S., Hernandez, P., and Golubic, E.: Multiwavelength aerosol lidars at the Maïdo supersite, Réunion Island, France: instrument description, data processing chain, and quality assessment, Earth System Science Data, 16, 4137–4159, https://doi.org/10.5194/essd-16-4137-2024, 2024.

Getzewich, B. J., Vaughan, M. A., Hunt, W. H., Avery, M. A., Powell, K. A., Tackett, J. L., Winker, D. M., Kar, J., Lee, K.-P., and Toth, T. D.: CALIPSO lidar calibration at 532 nm: version 4 daytime algorithm, Atmospheric Measurement Techniques, 11, 6309–6326, https://doi.org/10.5194/amt-11-6309-2018, 2018.

Godin-Beekmann, S., P. J. and Garnier, A.: Systematic DIAL lidar monitoring of the stratospheric ozone vertical distribution at Observatoire de Haute-Provence (43.92° N, 5.71° E), Journal of Environmental Monitoring, 5, 57–67, https://doi.org/https://doi.org/10.1039/B205880D, 2003.

Illingworth, A. J., Barker, H. W., Beljaars, A., Ceccaldi, M., Chepfer, H., Clerbaux, N., Cole, J., Delanoë, J., Domenech, C., Donovan, D. P., Fukuda, S., Hirakata, M., Hogan, R. J., Huenerbein, A., Kollias, P., Kubota, T., Nakajima, T., Nakajima, T. Y., Nishizawa, T., Ohno, Y., Okamoto, H., Oki, R., Sato, K., Satoh, M., Shephard, M. W., Velázquez-Blázquez, A., Wandinger, U., Wehr, T., and van Zadelhoff, G.-J.: The EarthCARE Satellite: The Next Step Forward in Global Measurements of Clouds, Aerosols, Precipitation, and Radiation, Bulletin of the American Meteorological Society, 96, 1311 – 1332, https://doi.org/10.1175/BAMS-D-12-00227.1, 2015.

Kar, J., Vaughan, M. A., Lee, K.-P., Tackett, J. L., Avery, M. A., Garnier, A., Getzewich, B. J., Hunt, W. H., Josset, D., Liu, Z., Lucker, P. L., Magill, B., Omar, A. H., Pelon, J., Rogers, R. R., Toth, T. D., Trepte, C. R., Vernier, J.-P., Winker, D. M., and Young, S. A.: CALIPSO lidar calibration at 532 nm: version 4 nighttime algorithm, Atmospheric Measurement Techniques, 11, 1459–1479, https://doi.org/10.5194/amt-11-1459-2018, 2018.

Khaykin, S. and Bourassa, A.: Atmospheric transport and evolution of Hunga water vapour and aerosols. In APARC, 2025: The Hunga Eruption Atmospheric Impacts Report [Yunqian Zhu, Graham Mann, Paul A. Newman, William Randel (Eds.)], Tech. Rep. APARC report No. 11, APARC IPO, https://doi.org/10.34734/FZJ-2025-05240, 2025.

https://doi.org/10.5194/egusphere-2026-2575
Preprint. Discussion started: 26 May 2026

Khaykin, S., Podglajen, A., Ploeger, F., Grooß, J.-U., Tence, F., Bekki, S., Khlopenkov, K., Bedka, K., Rieger, L., Baron, A., Godin-Beekmann, S., Legras, B., Sellitto, P., Sakai, T., Barnes, J., Uchino, O., Morino, I., Nagai, T., Wing, R., Baumgarten, G., Gerding, M., Duflot, V., Payen, G., Jumelet, J., Querel, R., Liley, B., Bourassa, A., Clouser, B., Feofilov, A., Hauchecorne, A., and Ravetta, F.: Global perturbation of stratospheric water and aerosol burden by Hunga eruption, Communications Earth & Environment, 3, 316, https://doi.org/10.1038/s43247-022-00652-x, 2022.

Khaykin, S., Sicard, M., Leblanc, T., Sakai, T., Balugin, N., Berthet, G., Chevrier, S., Chouza, F., Feofilov, A., Gantois, D., Godin-Beekmann, S., Haddouche, A., Jin, Y., Morino, I., Kadygrov, N., Lecas, T., Liley, B., Querel, R., Taha, G., and Yushkov, V.: Global transport of stratospheric aerosol produced by Ruang eruption from EarthCARE ATLID, limb-viewing satellites and ground-based lidar observations, Atmospheric Chemistry and Physics, 26, 607–622, https://doi.org/10.5194/acp-26-607-2026, 2026.

Klett, J. D.: Lidar inversion with variable backscatter/extinction ratios, Appl. Opt., 24, 1638–1643, https://doi.org/10.1364/AO.24.001638, 1985.

Kloss, C., Berthet, G., Sellitto, P., Bartolome Garcia, I., Briaud, E., Das, R. C., Chevrier, S., Dumelié, N., Joly, L., Lecas, T., Marbach, P., Ploeger, F., Renard, J.-B., Vernier, J.-P., Wienhold, F. G., and Hegglin, M. I.: Cross-Hemispheric Transport of the Hunga Aerosol Plume: In Situ Evidence and Radiative Effects from the Northern Hemisphere, EGUsphere, 2025, 1–24, https://doi.org/10.5194/egusphere-2025-2091, 2025.

Knepp, T. N., Kovilakam, M., Thomason, L., and Miller, S. J.: Characterization of stratospheric particle size distribution uncertainties using SAGE II and SAGE III/ISS extinction spectra, Atmospheric Measurement Techniques, 17, 2025–2054, https://doi.org/10.5194/amt-17-2025-2024, 2024.

Kokhanovsky, A.: Optical properties of terrestrial clouds, Earth-Science Reviews, 64, 189–241, https://doi.org/https://doi.org/10.1016/S0012-8252(03)00042-4, 2004.

Kremser, S., Thomason, L. W., von Hobe, M., Hermann, M., Deshler, T., Timmreck, C., Toohey, M., Stenke, A., Schwarz, J. P., Weigel, R., Fueglistaler, S., Prata, F. J., Vernier, J.-P., Schlager, H., Barnes, J. E., Antuña-Marrero, J.-C., Fairlie, D., Palm, M., Mahieu, E., Notholt, J., Rex, M., Bingen, C., Vanhellemont, F., Bourassa, A., Plane, J. M. C., Klocke, D., Carn, S. A., Clarisse, L., Trickl, T., Neely, R., James, A. D., Rieger, L., Wilson, J. C., and Meland, B.: Stratospheric aerosol—Observations, processes, and impact on climate, Reviews of Geophysics, 54, 278–335, https://doi.org/https://doi.org/10.1002/2015RG000511, 2016.

Lacour, A., Trapon, D., Dabas, A., Flament, T., Ehlers, F., and Huber, D.: Aeolus L2A Aerosol Optical Properties Product: Improvements and results, https://k-program.kuoni-congress.info/pdf/eumetsat-2022/presentation/aeolus-l2a-aerosol-optical-properties-product-improvements-and-results.pdf, 19–23 September 2022, Brussels, Belgium, EUMETSAT Meteorological Satellite Conference 2022 (last access: 21 January 2026), 2022.

Legras, B., Duchamp, C., Sellitto, P., Podglajen, A., Carboni, E., Siddans, R., Grooß, J.-U., Khaykin, S., and Ploeger, F.: The evolution and dynamics of the Hunga Tonga–Hunga Ha'apai sulfate aerosol plume in the stratosphere, Atmospheric Chemistry and Physics, 22, 14 957–14 970, https://doi.org/10.5194/acp-22-14957-2022, 2022.

Marseille, G. J. and Stoffelen, A.: Simulation of wind profiles from a space-borne Doppler wind lidar, Quarterly Journal of the Royal Meteorological Society, 129, 3079–3098, https://doi.org/https://doi.org/10.1256/qj.02.96, 2003.

Millán, L., Santee, M. L., Lambert, A., Livesey, N. J., Werner, F., Schwartz, M. J., Pumphrey, H. C., Manney, G. L., Wang, Y., Su, H., Wu, L., Read, W. G., and Froidevaux, L.: The Hunga Tonga-Hunga Ha'apai Hydration of the Stratosphere, Geophysical Research Letters, 49, e2022GL099 381, https://doi.org/https://doi.org/10.1029/2022GL099381, e2022GL099381 2022GL099381, 2022.

https://doi.org/10.5194/egusphere-2026-2575
Preprint. Discussion started: 26 May 2026

NASA/LARC/SD/ASDC: CALIPSO Lidar Level 1B profile data, V4-51 [data set], https://doi.org/10.5067/CALIOP/CALIPSO/CAL_LID_L1-Standard-V4-51.

Reitebuch, O., Krisch, I., Lemmerz, C., Lux, O., Schmidt, K., Witschas, B., Marksteiner, U., Rennie, M., Nikolaus, I., Fabre, F., Trapon, D., Dabas, A., Donovan, D., van Zadelhoff, G.-J., Wang, P., Marseille, G.-J., Kuijt, A., Tagliacarne, F., Perron, G., Huber, D., Meringer, M., Reissig, K., de Kloe, J., Cardaci, M., Gostinicchi, G., McLean, W., Henry, K., Benedetti, A., Bley, S., Stoffelen, A., Sabbatini, P., Mahfouf, J.-F., and Pourret, V.: The Earth Explorer Mission Aeolus for atmospheric wind observations - Final report from the Aeolus Data Innovation and Science Cluster DISC of Phase E, Tech. rep., ESA, https://elib.dlr.de/209970/, (last access: 17 January 2025), 2024.

Rennie, M., Tan, D., Andersson, E., Poli, P., Dabas, A., De Kloe, J., Marseille, G.-J., , and Stoffelen, A.: Aeolus Level-2B Algorithm Theoretical Basis Document (Mathematical Description of the Aeolus L2B Processor), Tech. rep., ESA, https://earth.esa.int/documents/d/earth-online/aeolus_l2b_algorithm_tbd-pdf, version 3.40 (last access: 20 May 2023), 2020.

Schoeberl, M. R., Wang, Y., Taha, G., Zawada, D. J., Ueyama, R., and Dessler, A.: Evolution of the Climate Forcing During the Two Years After the Hunga Tonga-Hunga Ha'apai Eruption, Journal of Geophysical Research: Atmospheres, 129, e2024JD041 296, https://doi.org/https://doi.org/10.1029/2024JD041296, e2024JD041296 2024JD041296, 2024.

Sellitto, P. and Legras, B.: Sensitivity of thermal infrared nadir instruments to the chemical and microphysical properties of UTLS secondary sulfate aerosols, Atmospheric Measurement Techniques, 9, 115–132, https://doi.org/10.5194/amt-9-115-2016, 2016.

Sellitto, P., Podglajen, A., Belhadji, R., Boichu, M., Carboni, E., Cuesta, J., Duchamp, C., Kloss, C., Siddans, R., Bègue, N., Blarel, L., Jegou, F., Khaykin, S., Renard, J.-B., and Legras, B.: The unexpected radiative impact of the Hunga Tonga eruption of 15th January 2022, Communications Earth & Environment, 3, 288, https://doi.org/10.1038/s43247-022-00618-z, 2022.

Sellitto, P., Belhadji, R., Legras, B., Podglajen, A., and Duchamp, C.: The optical properties of stratospheric aerosol layer perturbation of the Hunga volcano eruption of January 15th, 2022, EGUsphere, 2024, 1–19, https://doi.org/10.5194/egusphere-2024-1433, 2024a.

Sellitto, P., Siddans, R., Belhadji, R., Carboni, E., Legras, B., Podglajen, A., Duchamp, C., and Kerridge, B.: Observing the SO2 and Sulfate Aerosol Plumes From the 2022 Hunga Eruption With the Infrared Atmospheric Sounding Interferometer (IASI), Geophysical Research Letters, 51, e2023GL105 565, https://doi.org/https://doi.org/10.1029/2023GL105565, e2023GL105565 2023GL105565, 2024b.

Sicard, M., Baron, A., Ranaivombola, M., Gantois, D., Millet, T., Sellitto, P., Bègue, N., Bencherif, H., Payen, G., Marquestaut, N., and Duflot, V.: Radiative impact of the Hunga stratospheric volcanic plume: role of aerosols and water vapor over Réunion Island (21° S, 55° E), Atmospheric Chemistry and Physics, 25, 367–381, https://doi.org/10.5194/acp-25-367-2025, 2025.

Siddans, R., C.-E. S. P. and Legras, B.: RAL IMS retrieval of SO2 and sulphates (January to April 2022) (1.0.0), Zenodo [data set], https://doi.org/10.5281/zenodo.7102472, 2022.

Siddans, R.: Water Vapour Climate Change Initiative (WV-CCI) - Phase One, Deliverable 2.2, version 1.0, Tech. Rep. D2.2, STFC Rutherford Appleton Laboratory (RAL), 2019.

Sun, K., Dai, G., Trapon, D., Baars, H., Ansmann, A., Wandinger, U., and Wu, S.: Characterization of a huge transatlantic smoke transport event by constructing an Aeolus smoke dataset in synergy with multi-platform data, EGUsphere, 2026, 1–28, https://doi.org/10.5194/egusphere-2026-596, 2026.

Taha, G., Loughman, R., Colarco, P. R., Zhu, T., Thomason, L. W., and Jaross, G.: Tracking the 2022 Hunga Tonga-Hunga Ha'apai Aerosol Cloud in the Upper and Middle Stratosphere Using Space-Based Observations, Geophys Res Lett, 49, e2022GL100 091, 2022.

Trapon, D., Flament, T., Lacour, A., and Stieglitz, H.: Aeolus L2A user guide, Tech. rep., ESA, https://earth.esa.int/eogateway/documents/20142/37627/Aeolus-Data-Innovation-Science-Cluster-DISC-Level-2A-user-guide.pdf, version 2.2 (last access: 20 May 2023), 2022.

https://doi.org/10.5194/egusphere-2026-2575
Preprint. Discussion started: 26 May 2026

Trapon, D., Baars, H., Floutsi, A. A., Bley, S., Haarig, M., Lacour, A., Flament, T., Dabas, A., Nehrir, A. R., Ehlers, F., and Huber, D.: Cross-validations of the Aeolus aerosol products and new developments with airborne high-spectral-resolution lidar measurements above the tropical Atlantic during JATAC, Atmospheric Measurement Techniques, 18, 3873–3896, https://doi.org/10.5194/amt-18-3873-2025, 2025.

Vaughan, M. A., Young, S. A., Winker, D. M., Powell, K. A., Omar, A. H., Liu, Z., Hu, Y., and Hostetler, C. A.: Fully automated analysis of space-based lidar data: an overview of the CALIPSO retrieval algorithms and data products, in: Laser Radar Techniques for Atmospheric Sensing, edited by Singh, U. N., vol. 5575, pp. 16 – 30, International Society for Optics and Photonics, SPIE, https://doi.org/10.1117/12.572024, 2004.

Vérèmes, H., Payen, G., Keckhut, P., Duflot, V., Baray, J.-L., Cammas, J.-P., Evan, S., Posny, F., Körner, S., and Bosser, P.: Validation of the Water Vapor Profiles of the Raman Lidar at the Maïdo Observatory (Reunion Island) Calibrated with Global Navigation Satellite System Integrated Water Vapor, Atmosphere, 10, https://doi.org/10.3390/atmos10110713, 2019.

Winker, D., Hostetler, C., and Hunt, W.: Caliop: the Calipso LIDAR, 12-16 July, 2004 in Matera, Italy, 22nd Internation Laser Radar Conference (ILRC 2004), 2004.

Winker, D., Vaughan, M., and Hunt, B.: The CALIPSO mission and initial results from CALIOP, in: Lidar Remote Sensing for Environmental Monitoring VII, edited by Singh, U. N., Itabe, T., and Rao, D. N., vol. 6409, p. 640902, International Society for Optics and Photonics, SPIE, https://doi.org/10.1117/12.698003, 2006.

Winker, D. M., Pelon, J., Coakley, J. A., Ackerman, S. A., Charlson, R. J., Colarco, P. R., Flamant, P., Fu, Q., Hoff, R. M., Kittaka, C., Kubar, T. L., Treut, H. L., Mccormick, M. P., Mégie, G., Poole, L., Powell, K., Trepte, C., Vaughan, M. A., and Wielicki, B. A.: The CALIPSO Mission: A Global 3D View of Aerosols and Clouds, Bulletin of the American Meteorological Society, 91, 1211 – 1230, https://doi.org/10.1175/2010BAMS3009.1, 2010.

Wyser, K.: The Effective Radius in Ice Clouds, vol. 11, pp. 1793 – 1802, American Meteorological Society, Boston MA, USA, https://doi.org/10.1175/1520-0442(1998)011<1793:TERIIC>2.0.CO;2, 1998.

Xia, C., Liu, C., Cai, Z., Wu, H., Li, Q., and Gao, M.: Tracking SO2 plumes from the Tonga volcano eruption with multi-satellite observations, iScience, 27, 109 446, https://doi.org/https://doi.org/10.1016/j.isci.2024.109446, 2024.

Zhu, Y., Bardeen, C. G., Tilmes, S., Mills, M. J., Wang, X., Harvey, V. L., Taha, G., Kinnison, D., Portmann, R. W., Yu, P., Rosenlof, K. H., Avery, M., Kloss, C., Li, C., Glanville, A. S., Millán, L., Deshler, T., Krotkov, N., and Toon, O. B.: Perturbations in stratospheric aerosol evolution due to the water-rich plume of the 2022 Hunga-Tonga eruption, Communications Earth & Environment, 3, 248, https://doi.org/10.1038/s43247-022-00580-w, 2022.

Zhu, Y., Mann, G., Newman, P. A., and Randel, W.: The Hunga Volcanic Eruption Atmospheric Impacts Report, Tech. Rep. APARC report No. 11, APARC IPO, Jülich, https://doi.org/10.34734/FZJ-2025-05237, 2025.

https://doi.org/10.5194/egusphere-2026-2575
Preprint. Discussion started: 26 May 2026

Appendix A

A1 Data

A1.1 OPAR

The Observatory of Atmospheric Physics in Reunion (OPAR) is located in southwest of the Indian Ocean at La Reunion island where three ground-based lidars are operated since 2013 on a high altitude site (Maïdo mount, 2160 m a.s.l, [21.079° S-–55.383° E]): the Rayleigh Raman lidar (Li1200), the stratospheric ozone lidar and the tropospheric ozone lidar (LiO3T) (Gantois et al., 2024). The Li1200 provides vertical profiles of temperatures and water vapour ratio (Vérèmes et al., 2019) such as Rayleigh-Mie scattering at 355 nm. The aerosol extinction and backscatter coefficients can therefore be derived from the signals (Gantois et al., 2024) up to 40 km altitude with vertical resolution of 15 m. The LiO3S comes with DIfferential Absorption Lidar (DIAL) technique and measures ozone (O_3) concentration in the stratosphere between the tropopause and $\approx$ 45 km altitude (Godin-Beekmann and Garnier, 2003). Aerosol extinction and backscatter can also be retrieved from the elastic scattering at 355 nm (Gantois et al., 2024). The LiO3T also measures O_3 concentration in the troposphere with DIAL technique between 6 and 25 km (Duflot et al., 2017). Vertical profiles of aerosol extinction and backscatter can be retrieved from elastic scattering at 532 and 1064 nm. The two-component Klett inversion method (Klett, 1985) is used for the derivation of aerosol extinction and backscatter profiles for the three instrument (Gantois et al., 2024). The present study maskes use of the Li1200 and LiO3S aerosol profiles acquired on 25 January 2022.

A1.2 CALIOP

The Cloud-Aerosol Lidar with Orthogonal Polarization (CALIOP) was operated between April 2006 and June 2023 on board the CALIPSO satellite (Vaughan et al., 2004; Winker et al., 2010) flying at $\approx$ 700 km altitude. The CALIOP instrument is a lidar with two wavelength 532 nm and 1064 nm, and with a polarization channel. Among other products it measured the total attenuated 532 nm backscatter for molecules and particles $\beta^{\mathrm{att}}_{\mathrm{tot},532}$ as the perpendicular attenuated 532 nm backscatter for molecules and particles $\beta^{\mathrm{att}\perp}_{\mathrm{tot},532}$ with native resolution of 179.6 m vertical between $\approx$ 20.2 km and 30.1 km in altitude, and $\approx$ 333 m horizontal. The CALIOP lidar Level 1B (L1B) data product version 4.51 (V4.51) has been used. The 532 nm V4.51 data product relies on the calibration techniques explained in Kar et al. (2018) and Getzewich et al. (2018). The parallel-only attenuated 532 nm backscatter for particles and molecules $\beta^{\mathrm{att}\parallel}_{\mathrm{tot},532}$ is derived by subtracting $\beta^{\mathrm{att}\perp}_{\mathrm{tot},532}$ from $\beta^{\mathrm{att}}_{\mathrm{tot},532}$ to enable a comparison with Aeolus 355 nm SCA $\beta^{\mathrm{att}}_{\mathrm{tot}}$.

A1.3 IMS

The RAL (Rutherford Appleton Laboratory) and Infrared Microwave Sounder (IMS) scheme (Siddans, 2019) enables quantitative retrieval of sulphate-sepecific aerosol optical depth (Sellitto and Legras, 2016) and SO_2 concentration in parts per billion by volume (ppbv) from three instruments on board the MetOp platform: the Infrared Atmospheric Sounding Interferometer (IASI), the Advanced Microwave Sounding Unit (AMSU), and the Microwave Humidity Sounder (MHS). The RAL/IMS

https://doi.org/10.5194/egusphere-2026-2575
Preprint. Discussion started: 26 May 2026

makes use of optimal estimation with signal acquired in the mid infrared region between 1100 and 1200 cm^{-1} (Clerbaux et al., 2009), and assuming a uniform vertical mixing ratio. Both quality controlled products are referred as IMS SA OD and IMS SO_2 in the present study. They comes with a 0.25° regular grid in latitudes and longitudes. Both daytime and nighttime swaths have been used to calculate weekly average map.

A1.4 Aeolus ready-to-use cloud mask

The L2A product labelled Baseline 16 includes a cloud mask based on model data from the European Centre for Medium-Range Weather Forecasts (ECMWF). A total cloud backscatter β_{tot} is estimated via a simple parametrization using cloud liquid and ice water content taken from the Auxiliary Meteorological Data (AUX_MET) and a threshold is applied. The cloud mask therefore helps to discriminate aerosols from the clouds predicted by the ECMWF short-range numerical weather prediction (NWP) forecast, and is given at the coarser resolution observation of $\approx 90\ \mathrm{km}$, then corresponding to 15 consecutive SCA measurements and 3 consecutive MLEsub profiles for the period 13 December 2021 to 04 April 2022. As described with the Eqs. (8.1) and (8.2) of the L2A ATBD (Flamant et al., 2022) shown below with Eqs. A1 and A2, the extinction coefficients for liquid water clouds α_{water} and ice clouds α_{ice} in m^{-1} are firstly calculated according to the Mie theory as explained in Kokhanovsky (2004). Liquid and ice water content LWC and IWC, respectively in $\mathrm{kg/kg}$, are extracted from the AUX_MET. Liquid and ice water effective radius, $r_{\mathrm{e,LW}}$ and $r_{\mathrm{e,IW}}$ respectively in m, liquid and ice water density at 0 $°C$ ρ_{LW} and ρ_{IW} respectively equal to 999.8395 kgm^{-3} and 916.7 kgm^{-3}, and air density ρ in kgm^{-3} :

$$\alpha_{\mathrm{water}} = \frac{3}{2}\frac{LWC\rho}{r_{\mathrm{e,LW}}\rho_{\mathrm{LW}}} \tag{A1}$$

$$\alpha_{\mathrm{ice}} = \frac{3}{2}\frac{IWC\rho}{r_{\mathrm{e,IW}}\rho_{\mathrm{IW}}} \tag{A2}$$

The air density ρ is derived from nominal pressure p in hPa, temperature T in K, and specific gas constant for dry air R equal to 287.058 $\mathrm{JK}^{-1}\mathrm{kg}^{-1}$, as shown with Eq. (8.3) of Flamant et al. (2022):

$$\rho = \frac{p}{RT} \tag{A3}$$

$r_{\mathrm{e,LW}}$ is calculated with Eq. A4 below adapted from the parametrization of Eq. (5) of Marseille and Stoffelen (2003) which has been adopted from the ECMWF forecast model (i.e. stating that the mean droplet size in low-level clouds is smaller than in high-level clouds), with P the air pressure in hPa:

$$r_{\mathrm{e,LW}} = (-3.8 \times 10^{-2} P + 43.8 \times 10^{-6}) \tag{A4}$$

$r_{\mathrm{e,IW}}$ is derived from Eqs. A5 and A6 below adapted from Eqs. (35) and (14) of Wyser (1998):

$$r_{\mathrm{e,IW}} = 377.4 + 203.3B + 37.91B^2 + 2.3696B^3, \tag{A5}$$

$$B = -2 + 1.0 \times 10^{-3} \frac{\left((273 - T)^{\frac{3}{2}}\right) \times \frac{log(IWC\rho)}{50}}{log(10)}. \tag{A6}$$

https://doi.org/10.5194/egusphere-2026-2575
Preprint. Discussion started: 26 May 2026

The total cloud backscatter β_{tot} in $\text{m}^{-1}\text{sr}^{-1}$ is derived from total extinction being the sum of α_{water} and α_{ice}, and using a constant LR equal to 20 sr:

$$\beta_{\text{tot}} = \frac{\alpha_{\text{water}} + \alpha_{\text{ice}}}{LR} \tag{A7}$$

The bins are considered contaminated by clouds if β_{tot} is superior to a threshold of 1.0×10^{-7} $\text{m}^{-1}\text{sr}^{-1}$ which was determined by the L2A development team with sensitivity test. The cloud mask helps discarding all bins that include signal from water or ice clouds. Examples of the cloud screening removal are given in (Trapon et al., 2022) in section 4.8. In this study, the cloud mask was applied to the following L2A product: SCA $\beta_{\text{tot}}^{\text{att}}$ and MLEsub α_{part}, β_{part}, LR, SR and LOD.

A2 Result

A2.1 IMS weekly average map

https://doi.org/10.5194/egusphere-2026-2575
Preprint. Discussion started: 26 May 2026

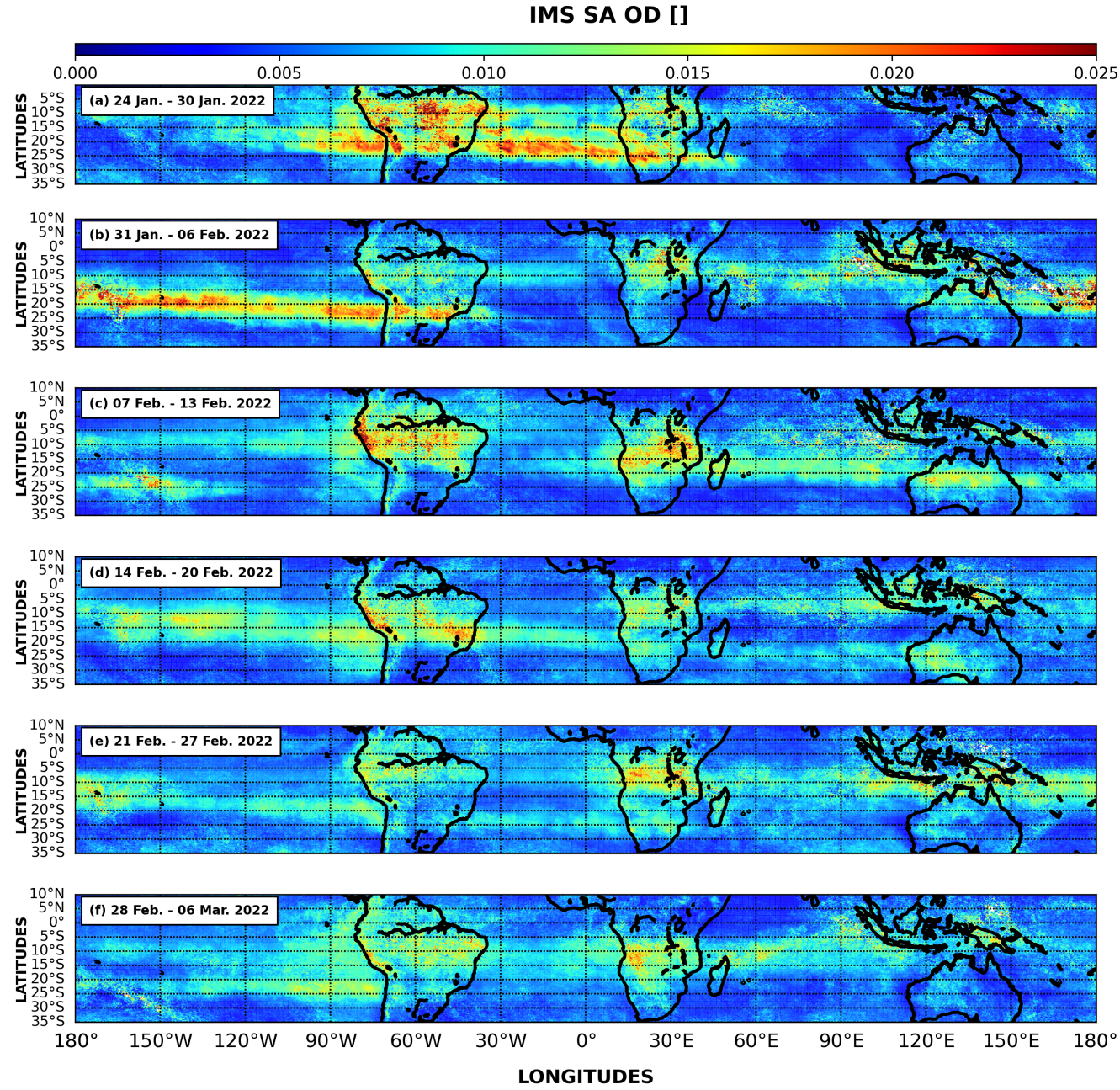

Figure A1. Weekly average of IMS SA OD for daytime and nighttime swaths. The time progresses from right to left. The panels a-f correspond to the 6 weeks of the period from 24 January 2022 to 06 March 2022.

https://doi.org/10.5194/egusphere-2026-2575
Preprint. Discussion started: 26 May 2026

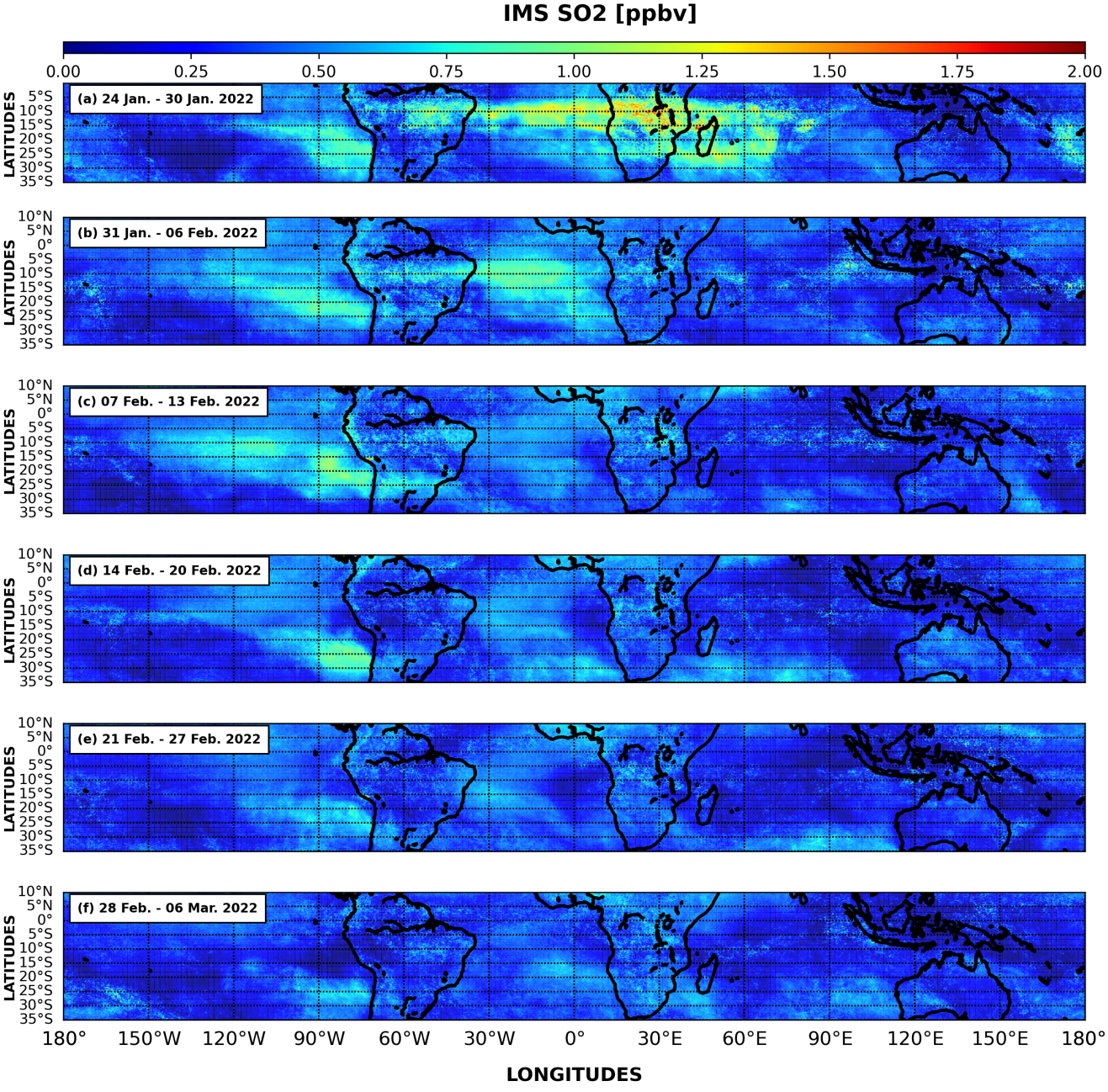

Figure A2. Weekly average of IMS SO_2 for daytime and nighttime swaths. The time progresses from right to left. The panels a-f correspond to the 6 weeks of the period from 24 January 2022 to 06 March 2022.

https://doi.org/10.5194/egusphere-2026-2575
Preprint. Discussion started: 26 May 2026

A2.2 Aeolus two-dimensional histograms

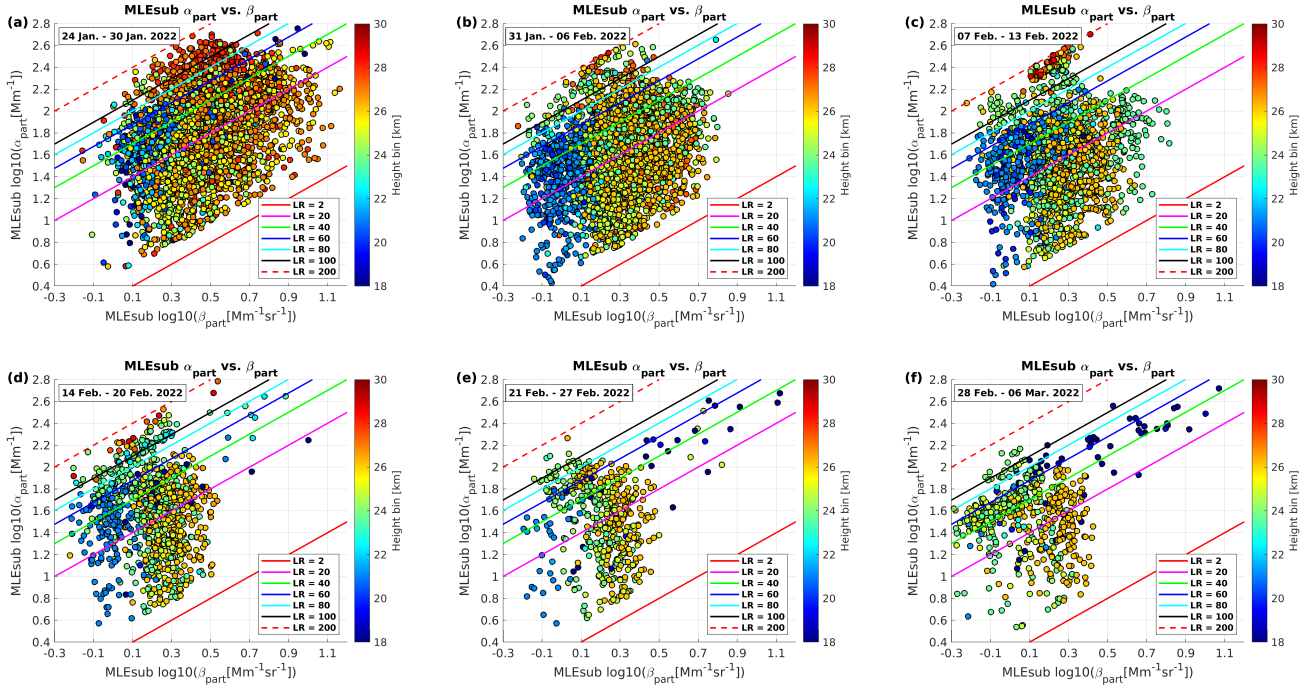

Figure A3. Two-dimensional histograms of Aeolus L2A α_{part} versus β_{part} for every range bin where the maximum column value SR is detected. The height bin is shown by varying colours. The L2A QC, cloud mask, and SR threshold of 2 are applied. The panels a-f correspond to the 6 weeks of the period from 24 January 2022 to 06 March 2022.

https://doi.org/10.5194/egusphere-2026-2575
Preprint. Discussion started: 26 May 2026

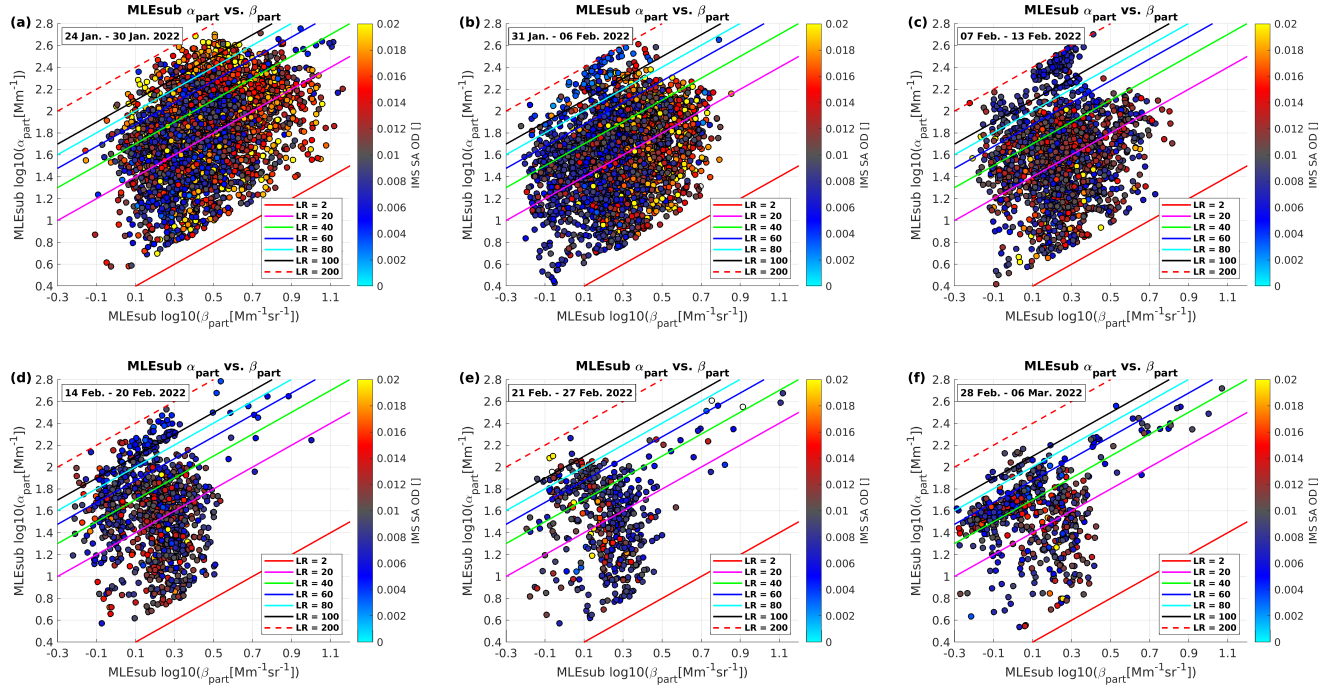

Figure A4. Two-dimensional histograms of Aeolus L2A α_{part} versus β_{part} for every range bin where the maximum column value SR is detected. The IMS SA OD is shown by varying colours. The L2A QC, cloud mask, and SR threshold of 2 are applied. The panels a-f correspond to the 6 weeks of the period from 24 January 2022 to 06 March 2022.

https://doi.org/10.5194/egusphere-2026-2575
Preprint. Discussion started: 26 May 2026

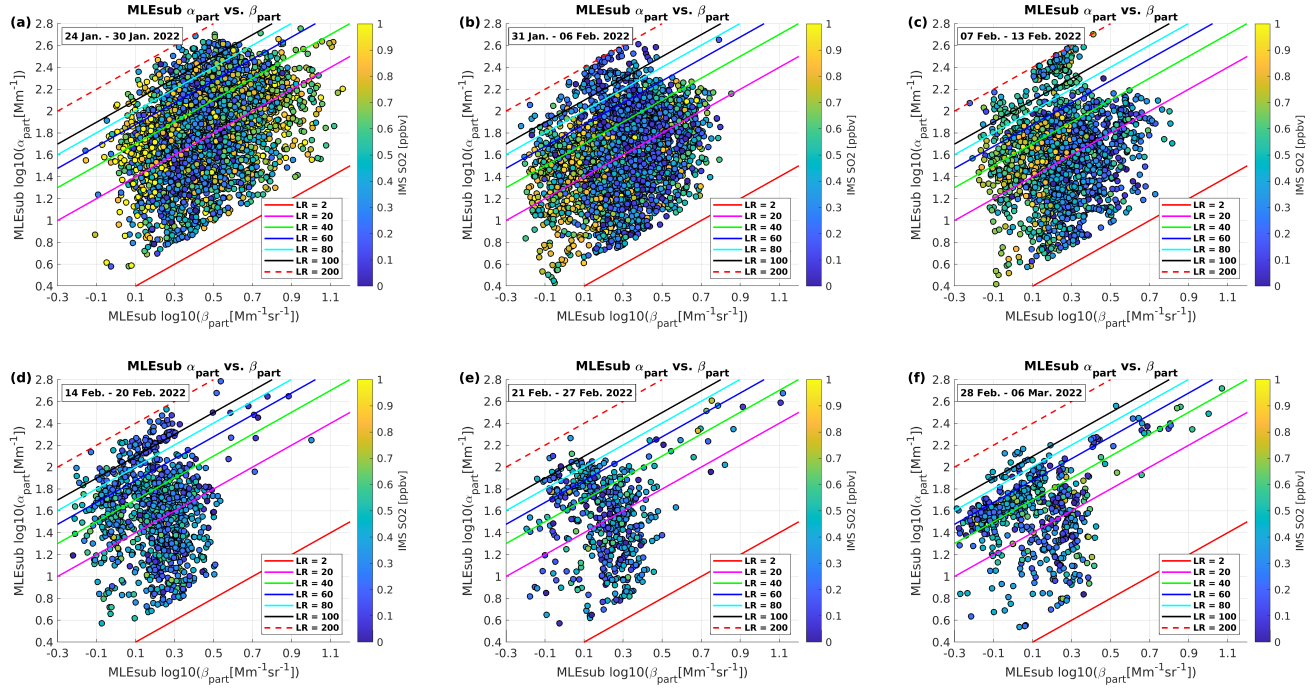

Figure A5. Two-dimensional histograms of Aeolus L2A α_{part} versus β_{part} for every QC flagged range bin where the maximum column value SR is detected. The IMS SO_2 is shown by varying colours. The L2A QC, cloud mask, and SR threshold of 2 are applied. The panels a-f correspond to the 6 weeks of the period from 24 January 2022 to 06 March 2022.